PHYSICAL REVIEW D VOLUME 24, NUMBER 11 1 DECEMBER 1981

# Exclusive $\rho^0$, $\omega$, and $\phi$ electroproduction

D. G. Cassel, L. A. Ahrens,* K. Berkelman, C. T. Day,†
B. G. Gibbard,* D. J. Harding,‡ D. L. Hartill,
J. W. Humphrey,* T. J. Killian,* J. S. Klinger,§
J. T. Linnemann,|| R. A. Perchonok, E. A. Treadwell,‡ and D. H. White*
*Laboratory of Nuclear Studies, Cornell University, Ithaca, New York 14853*

(Received 22 May 1981)

We have measured exclusive $\rho^0$, $\omega$, and $\phi$ meson electroproduction at the Cornell Wilson Synchrotron. The final $\rho^0$ data sample included 4637 four-constraint $e+p\rightarrow e+\pi^+ +\pi^- +p$ events, with incident energy $E=11.5$ GeV and electroproduction variables $Q^2$ and $W$ in the region $0.7<Q^2<4$ GeV$^2$ and $1.9<W<4$ GeV. We find that the width of the forward $\rho^0$ diffraction peak increases rapidly as the lifetime of the intermediate hadron states decreases below $c\Delta\tau=1$ fm and that the peak is wider for longitudinal $\rho^0$ than it is for transverse $\rho^0$. The longitudinal-transverse cross-section ratio $R_\rho=\sigma_L/\sigma_T$, obtained assuming $s$-channel helicity conservation, becomes constant at high $Q^2$. At fixed $W$ the diffractive vector-meson-dominance (VMD) model reproduces the $Q^2$ dependence of our cross section, $\sigma=(\sigma_T+\epsilon\sigma_L)$, but is is not able to account for the rapid decrease in the cross section with increasing $W$ we observe. We find that $\sigma_\omega/\sigma_\rho$ depends on $W$ but is independent of $Q^2$ for $0.7<Q^2<3$ GeV$^2$ and $2.2<W<3.7$ GeV. However, $\sigma_\omega$ is substantially larger than the diffractive VMD cross section. Our results for $\sigma_\phi$ are consistent with the $Q^2$ dependence of the diffractive VMD model for $0.8<Q^2<4$ GeV$^2$ and $2<W<3.7$ GeV, but this model again fails to predict the $W$ dependence we observe.

## I. INTRODUCTION

In this paper we present the final results of a vector-meson electroproduction experiment at the Cornell Wilson Synchrotron laboratory. We have previously published preliminary results[1,2] on $\rho^0$ and a brief report[3,4] on $\omega$ electroproduction. This is the first publication of our $\phi$ electroproduction data.[5]

The results of a long series of photoproduction and electroproduction experiments and their theoretical interpretation are summarized in an excellent review.[6] The results of these experiments are usually compared to the predictions of the vector-meson-dominance (VMD) model. Briefly, the VMD model assumes that vector-meson production by real or virtual photons is dominated by the scattering of the vector-meson components of the virtual hadrons present in the internal structure of high-energy photons. The simplest and most common VMD model assumes that scattering is diffractive. This diffractive mechanism implies that vector mesons should be produced in a forward peak reminiscent of diffractive hadron scattering, that the high-energy cross section should be largely independent of the total photon-proton ($\gamma p$) center-of-mass energy $W$, and that the helicity of the incident photon should be transferred to the vector meson. Photoproduction experiments generally agree well with these predictions.[6]

It is natural to assume that this behavior persists in electroproduction as $Q^2$ increases. ($Q^2$ is minus the electron four-momentum transfer squared.) In addition, the cross section should decrease approximately as the square of the vector-meson propagator as $Q^2$ increases, and the width of the forward peak should increase as the formation time[7] of the virtual intermediate hadron states decreases below $c\Delta\tau=1$ fm. Electroproduction experiments generally agreed that the cross section decreases with $Q^2$ as expected, but the increase in the width of the diffraction peak remained controversial.[6]

Apart from vector-meson photoproduction and electroproduction, the VMD model successfully describes the total $\gamma p$ cross section and Compton scattering at $Q^2=0$, but it is not nearly as successful in the deep-inelastic region where the total cross section is much better represented by the quark-parton model. An eventual synthesis of the VMD and quark-parton models should include predictions for the behavior of vector-meson electroproduction in the region of transition between the two models.[8] We explore the transition region in this experiment.

Electroproduction experiments have been limited by poor statistics, low $Q^2$ and $W$, or by the observation of only one or two of the final-state hadrons (which leads to potential uncertainties in the backgrounds). The present experiment removes all of these constraints. We have accumulated data in a large-aperture-magnet experiment (LAME)[9] at the Cornell Wilson Synchrotron. The scattered electron and proton, and the charged hadrons resulting from vector-meson decay were detected in this spectrometer. The solid-angle acceptance for the detector implied an average probability of 60% for detecting a charged hadron. With this hadron solid angle, we were able to accumulate a large number of events in which all charged particles in the final state were detected.

In these experiments, the incident electron energy was $E=11.5$ GeV. In the $\rho^0$ electroproduction experiment the data presented cover the ranges $0.7<Q^2<4$ GeV$^2$ and $1.9<W<4$ GeV. The $Q^2$-$W$ limits in the $\omega$ and $\phi$ experiments are similar. The final data sample used in obtaining the $\rho^0$ electroproduction cross section included 4637 events with four final-state particles detected, which were consistent with the four-constraint (4C) hypothesis $e+p\rightarrow e+\pi^+ +\pi^- +p$.

In Sec. II, we review the kinematics and electroproduction phenomenology common to $\rho^0$, $\omega$, and $\phi$ electroproduction. Aspects of the experiment common to the three reactions, the aparatus and data taking, the data-reduction programs, and the acceptance and efficiency calculations are outlined in Secs. III, IV, and V, respectively. We devote Sec. VI to the analysis used to extract the $\rho^0$ cross section from the data. In Sec. VII, we present the results for $\rho^0$ electroproduction. The $\omega$ and $\phi$ analyses are substantially simpler, and are presented with results in Secs. VIII and IX, respectively. Section X is a summary of the results and conclusions.

## II. KINEMATICS AND CROSS SECTIONS

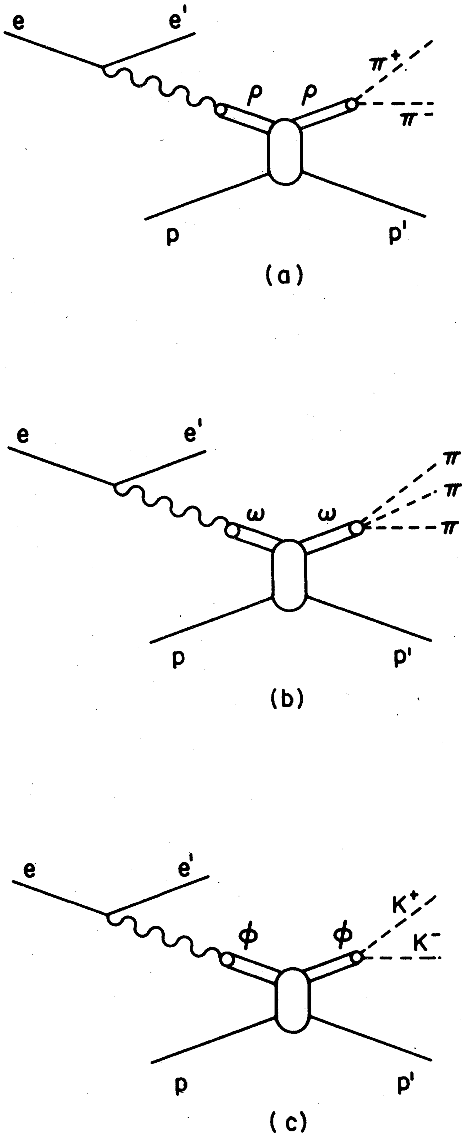

FIG. 1. The one-photon-exchange diagrams for diffractive $\rho^0$, $\omega$, and $\phi$ electroproduction and their decay into the hadrons observed in this experiment.

Figure 1 illustrates the one-photon-exchange diagrams for $\rho^0$, $\omega$, and $\phi$ electroproduction and their decays into the hadrons that we observed. Using standard notation,[10] $E$ and $E'$ are the incident- and scattered-electron energies, $\theta_e$ is the electron scattering angle, and $M$ is the mass of the proton. Neglecting the electron mass, the kinematic variables for the virtual photon $\gamma_V$ are determined by its energy $\nu=E-E'$ and $Q^2=4EE'\sin^2(\theta_e/2)$, which is minus the electron four-momentum transfer. The virtual-photon—proton ($\gamma_V p$) center-of-mass energy $W$ is $W^2=-Q^2+M^2+2M\nu$. The total cross section for electroproduction of a vector meson is given by the familiar expressions due to Hand[11] and Akerlof *et al.*,[12]

$$\frac{d^3\sigma_e}{d\Omega_e dE'}=\Gamma_T(E,E',\theta_e)[\sigma_T(Q^2,W)+\epsilon\sigma_L(Q^2,W)] . \quad (1)$$

In this expression, $\Gamma_T$ is the flux of transverse virtual photons

$$\Gamma_T(E,E',\theta_e)=\frac{\alpha}{4\pi^2}\frac{E'}{E}\frac{W^2-M^2}{MQ^2}\frac{1}{1-\epsilon} \tag{2}$$

and $\epsilon$ is the virtual-photon polarization parameter

$$\epsilon=\frac{1}{\{1+2[(Q^2+\nu^2)/Q^2]\tan^2(\theta_e/2)\}} . \tag{3}$$

The cross section

$$\sigma(Q^2,W)=\sigma_T(Q^2,W)+\epsilon\sigma_L(Q^2,W) \tag{4}$$

is the total cross section for production of the vector meson by a virtual photon specified by $Q^2$ and $W$. $\sigma_T$ is the contribution from unpolarized transverse photons, and $\sigma_L$ is the contribution from longitudinal photons.

The invariants $Q^2$ and $W$ are more closely related to the virtual photon than are $E'$ and $\theta_e$, so it is useful to reexpress the cross section of Eq. (1) as differential in $Q^2$ and $W$. After multiplying by the Jacobian

$$J(\cos\theta_e,E' \mid Q^2,W)=\frac{W}{2MEE'} , \tag{5}$$

Eq. (1) becomes

$$\frac{d^2\sigma}{dQ^2dW\,d\phi_\gamma}=\Gamma_W(Q^2,W)[\sigma_T(Q^2,W)+\epsilon\sigma_L(Q^2,W)] , \tag{6}$$

where $\phi_\gamma$ is the azimuthal angle of the virtual photon and

$$\Gamma_W(Q^2,W)=\frac{\alpha}{8\pi^2}\frac{W}{ME^2}\frac{W^2-M^2}{MQ^2}\frac{1}{1-\epsilon} . \tag{7}$$

$\theta_e$ can also be eliminated from $\epsilon$ in Eq. (3) to give

$$\epsilon=\frac{1}{[1+2(Q^2+\nu^2)/(4EE'-Q^2)]} . \tag{8}$$

Neglecting interference, the cross section for observing a particular set of final-state hadrons is given by a sum of terms of the form of Eq. (6), each term representing a particular reaction channel. The separation of the specific vector-meson-production channels from other resonant and nonresonant channels is described in Secs. VI–IX.

## III. THE APPARATUS AND DATA TAKING

The design and performance of the LAME apparatus is described in detail elsewhere,[2,4,5,9,13–16] so we include only a brief summary here. Electrons were accelerated to a nominal energy of $E_0=11.5$ GeV at a repetition rate of 60 Hz in the Cornell Wilson Synchrotron. They were extracted using resonant extraction over a time interval of approximately $\pm 1$ msec surrounding the peak of the magnet cycle. Over this spill width, the beam energy varied between 0.98 $E_0$ and $E_0$; the incident energy for each event was determined by measuring the time of the event relative to the peak of the magnet cycle. The beam was brought to the detector in a beam-transport system carefully optimized to reduce halo in the detector. Typical beams delivered to the experiment had $5\times10^7$ electrons/sec in a spot of approximately 1.5 mm full width at half maximum (FWHM) and an angular divergence of about $\pm 1$ mrad. The halo rate for such a beam was approximately 5 Hz outside a diameter of 8 cm. It was possible to position the beam with an accuracy of $\pm 0.5$ mm and to fix its angle to an accuracy of $\pm 1$ mrad using a set of beam profile chambers in the detector.

The detector is illustrated in Fig. 2. The beam traveled through a large dipole magnet (Brookhaven Type 96D40) passing through holes in 5-cm iron shims inserted in the median plane of the yoke. It was incident on a 7.5-cm-long-by-1.9-cm-diameter liquid-hydrogen target. The unscattered electron beam was absorbed in a calibrated laboratory standard secondary-emission quantameter (SEQ). The SEQ current was integrated by a specially designed integrator[15] accurate to $\pm 1\%$, and the resulting charge was scaled and written on the output tape in special even records. The central field of the magnet was 8.5 kG. It was rather nonuniform near the edges of the $244\times102\times61$ cm gap. Extensive field maps were required for accurate determination of particle momentum. They were measured and analyzed following Wind's suggestions.[17]

Charged particles were detected within the magnetic-field volume in 34 planes of proportional wire chambers,[2] arranged in 14 chambers as shown in Fig. 2. These chambers were carefully designed to minimize mass and maximize solid angle. They were operated with a "magic gas"[4,18] mixed locally. The downstream chambers were oriented at 90° to the $z$ axis which coincided with the incident-electron-beam direction; the rest were oriented at $\pm 30°$ to the $z$ axis. The seven chambers on one side of the $z$ axis contained seven $U$ planes to measure horizontal coordinates, six $V$ planes to measure vertical coordinates, and four $W$ planes with wires at 30° to the vertical to resolve ambiguities.

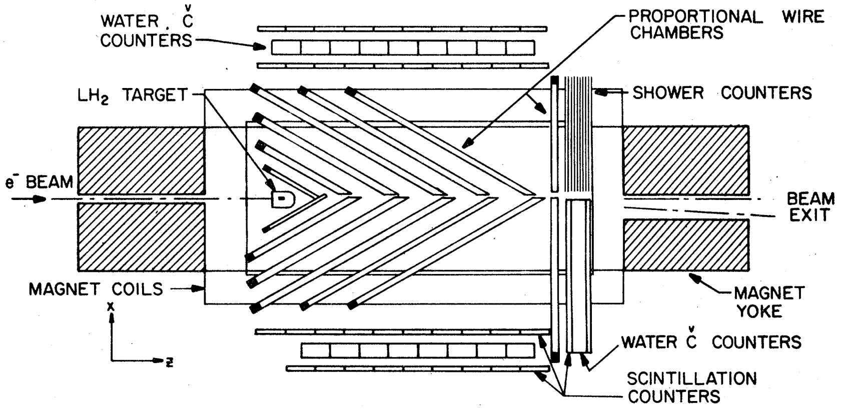

FIG. 2. The LAME detector viewed from above.

There were a total of 21 000 wires spaced 1.5 mm apart in these chambers. The momentum resolution of the system was $\sigma_p/p \cong 0.015p$ ($p$ in GeV). The chambers were carefully designed with dead regions in the median plane where the unscattered electron beam exited from the magnet through the chambers, and where the degraded electrons and the $e^+e^-$ pairs produced in the target were fanned out by the magnetic field.

The experiment was triggered by the lead-scintillator shower counters shown in Fig. 2. Their transverse distance from the unscattered electron beam determined the minimum $Q^2$ (${Q^2}_{\text{min}}$) for accepted electrons. During most of the data-taking run, ${Q^2}_{\text{min}}$ was 0.5 GeV$^2$, but it was 0.7 GeV$^2$ for part of the run. The counter was split into two halves above and below the median plane to eliminate the background due to positrons swept into the counter region by the magnetic field. The photomultiplier gains were monitored and adjusted during the runs using a light-emitting-diode system. The experiment was triggered by a pulse in the shower counter corresponding to a threshold scattered electron energy $E'_{\text{min}} = 2.5$ GeV. The shower-counter efficiency[2] as a function of $E'$ is illustrated in Fig. 3. The counter was more than 90% efficient for $E' > 3$ GeV. Figure 4 shows the $Q^2$-$W$ bins used in the $\rho^0$ experiment, along with curves of constant $E'$. Although the $E' = 3$ GeV curve cuts across the $Q^2$-$W$ region used in the experiment, vector-meson cross sections in the affected region are small. We have included this small inefficiency effect in the Monte Carlo calculation described in Sec. V.

The time-of-flight scintillation counters and water Čerenkov counters shown in Fig. 2 were used for hadron identification[16] and were not involved in the trigger. They were not used in the analysis of $\rho^0$ and $\phi$ electroproduction because the constrained kinematic fits described later made the counter information redundant. These counters were used in the $\omega$ experiment as described in Sec. VIII.

A specially designed readout system transferred data from the 21 000 proportional wires and 144 photubes, as well as scalar and other monitoring data, to an on-line PDP 11 computer.[19] Because of the large number of channels, the system was optimized for speed and low cost. The data for an event could be transferred in the ~17 msec between beam pulses. The PDP 11 computer reformatted the data, monitored a variety of performance indicators, provided a software trigger, and wrote satisfactory events onto magnetic tape. The PDP 11 first rejected events with too many input

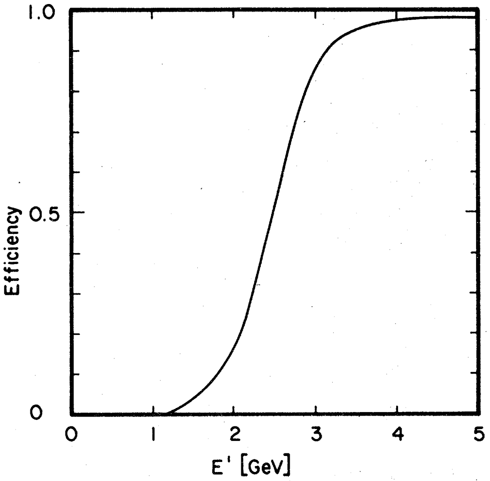

FIG. 3. The efficiency of the trigger shower counter as a function of scattered electron energy $E'$.

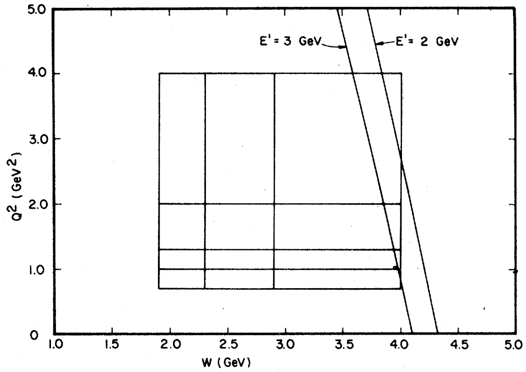

FIG. 4. A plot of the $Q^2$-$W$ bins used in our $\rho^0$ experiment along with the curves corresponding to constant values of $E'$ equal to 2 and 3 GeV.

words. Then it searched for negatively charged tracks headed towards the shower counters. Events that passed this track-finding cut were written onto a tape along with a small sample of events independent of this cut. After 128 normal data events were written, a special event record containing information that was necessary for obtaining normalized cross sections and performance monitoring was written. The record contained the integrated SEQ current and gated and ungated rates in the shower counter. These rates were used to calculate the number of electrons incident on the target during the live time of the experiment. We recorded a total of $5.0\times10^{14}$ electrons during the experiment live time.

## IV. EVENT RECONSTRUCTION

We used a PDP 10 KI processor[19] for the offline event reconstruction. The analysis was divided into distinct passes[9] with output tapes written after each pass. The first pass involved track finding[13] in a uniform field approximation with large road widths to compensate for the field nonuniformities. Tracks were first found using the $U$ and $V$ planes separately. The track finding was biased towards, but not restricted to, tracks coming from the center of the target. The $U$ and $V$ tracks were then combined with the pairing determined by the $W$ planes. In a further step,[5] we examined the tracks found by this program and eliminated absurd strikes and combined tracks apparently coming from the same particle. The cuts were kept rather loose to ensure that all reasonable tracks were found; wild hits and tracks with mostly wild hits were eliminated at a later stage.

The second-pass analysis produced a least-squares fit of all tracks in an event to a common vertex.[14] This global fit was made with tables, which mapped the track momentum vector into the coordinates and certain derivatives of the coordinates in each chamber plane. These tables were derived from the measured magnetic-field maps so they implicitly corrected for the nonuniformities in the magnetic field. The fit was iterated after removing hits not consistent with the overall fit. For each event, this pass provided an event vertex, track momenta, and the full error matrix for the output tape. Approximately $10^5$ events had four tracks with no missing charge, and were therefore candidates for the reactions discussed in this paper. Elsewhere[20] we explain in detail how events are lost as they proceed through the reconstruction stream.

In this experiment, photons were not detected, so the $\pi^0$ from $\omega\rightarrow\pi^+ + \pi^- + \pi^0$ decay was not observed. Hence, the signatures for $\rho^0$, $\omega$, and $\phi$ electroproduction were the same, since all three production and decay reactions

$$\begin{aligned}&e+p\rightarrow e+\rho^0+p\\&\qquad\quad\searrow \pi^+ + \pi^- ,\end{aligned}\tag{9a}$$

$$\begin{aligned}&e+p\rightarrow e+\omega+p\\&\qquad\quad\searrow \pi^+ + \pi^- + \pi^0 ,\end{aligned}\tag{9b}$$

$$\begin{aligned}&e+p\rightarrow e+\phi+p\\&\qquad\quad\searrow K^+ + K^- ,\end{aligned}\tag{9c}$$

resulted in two positive and two negative particles appearing in the final state. The electron was uniquely identified by matching the negative tracks with the shower-counter signals. The hadron final states $(p\pi^+\pi^-)$, $(p\pi^+\pi^-\pi^0)$, and $(pK^+K^-)$ were separated with kinematic fitting. We describe the isolation of the $\omega$ events using a one-constraint (1C) fit in Sec. VIII. In order to identify the $\rho^0$ and $\phi$ events, we used a novel approach which we have previously described.[9,20,21] Briefly, we first subjected the events with two positive and two negative tracks to a three-constraint (3C) fit, using three-momentum conservation as the constraints. Approximately 15 000 events satisfied this fit with $\chi^2 < 20$ for three degrees of freedom. Since the electron was identified in the shower counter, the only remaining ambiguities were the identity of the proton, and the assignment of the labels $\pi$, $K$, or $p$ to the other two hadrons. After the recoil proton was assigned, the two other hadrons $(X^+, X^-)$

must have had the same mass, if strangeness and baryon number were conserved.

Therefore, we were able to use energy conservation to calculate the mass $m_X$ of these two remaining hadrons. In 85% of the events a real solution for $m_X$ was obtained for only one of the two possible choices of a positive track as the proton. In the other 15% of the events, where both positive tracks gave a real solution for $m_X$, we chose the solution nearer a real particle mass $m_\pi$, $m_K$, or $M$ (the charged-$\pi$, charged-$K$, and $p$ mass, respectively). The resulting mass distributions are shown in Fig. 5. About 10 000 events had $m_X$ sufficiently near $m_\pi$, $m_K$, or $M$. We then subjected each event with $\chi^2 < 20$ from the 3C fit to a 4C fit using the mass assigned by the 3C fits. We then included events with the $\chi^2$ from the 4C fit less than 40 in the final data sample. Figure 6 shows how the 4C fit was highly effective in removing background from the $(pK^+K^-)$ sample. Figure 7 is a typical $e+p \rightarrow e+\rho^0+p$ candidate selected by this analysis.

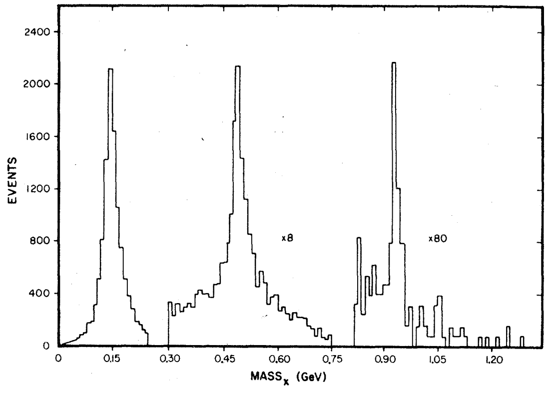

FIG. 5. $m_X$ distributions where events are assumed to be $e+p \rightarrow e+X^+ + X^- + p$. (Note that the $K^+K^-$ and $p\bar{p}$ data have been multiplied by factors of 8 and 80, respectively.)

## V. ACCEPTANCE AND EFFICIENCY CALCULATIONS

We used a special subroutine CHEFF[4] to monitor the proportional-chamber efficiencies throughout

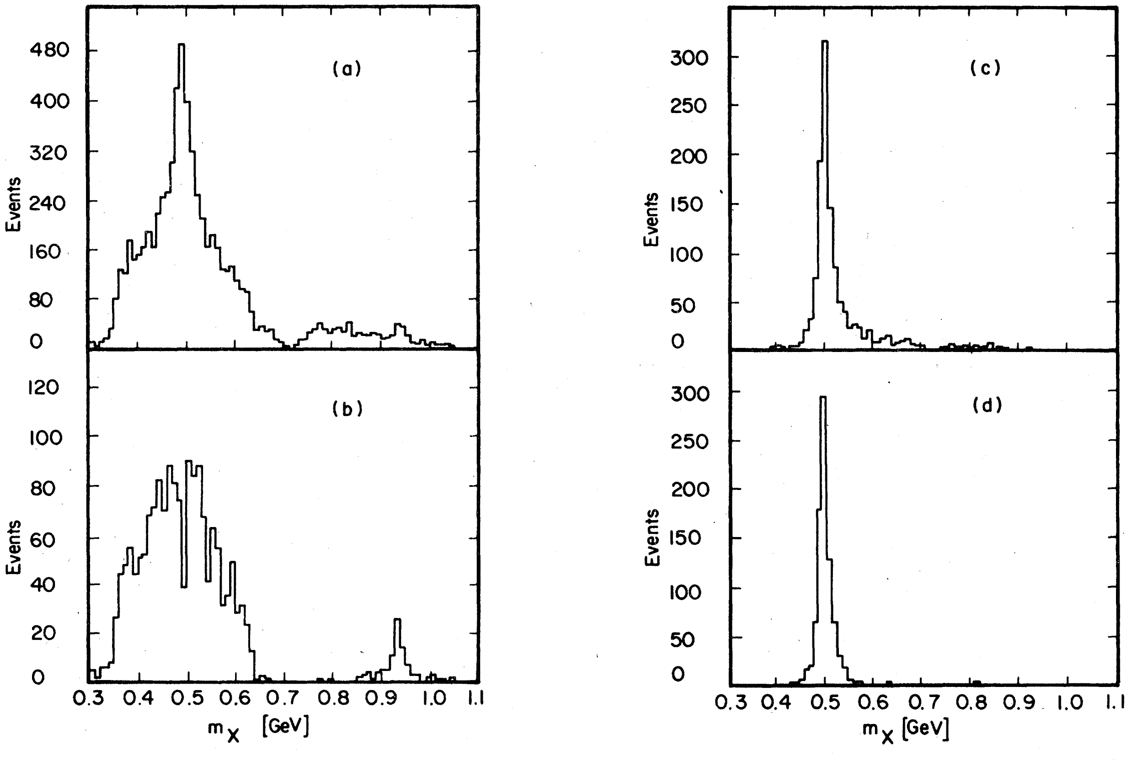

FIG. 6. The effect of the 4C fit on the 3C $K^+K^-$ sample. $m_X$ is the mass determined from the 3C fit. (a) shows the $m_X$ spectrum for $m_X > 0.3$ GeV with $\chi^2 < 25$, before the 4C fit. The events in (b) are ones in which the $K^+K^-$ hypothesis did not give the smallest 4C $\chi^2$, while those in (c) had a lower 4C $\chi^2$ for the $K^+K^-$ hypothesis than for either the $\pi^+\pi^-$ or $p\bar{p}$ hypotheses. (d) shows the events in (c) with 4C $\chi^2 < 40$.

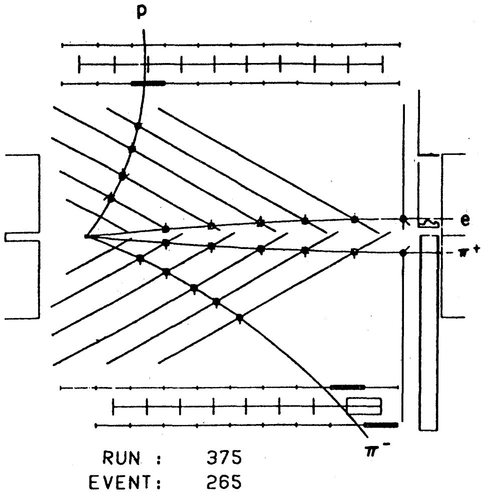

FIG. 7. A typical $\rho^0$ electroproduction candidate. The $\pi^+\pi^-$ effective mass is $m_{\pi\pi}=750$ MeV in this event. The tracks are shown and labeled. The proportional chambers are shown with tick marks indicating hits. The small histograms in the shower-counter region show that the electron entered the lower of the two counters. The rectangles in the time-of-flight counters show that the $p$ and $\pi^-$ were observed there. Note that the slow $p$ was absorbed in the water Čerenkov counter and did not count in the rear timing counter.

the data-taking runs. CHEFF was called for a sample of the events after completion of track finding and elimination of obvious bad hits and tracks. CHEFF first selected a set of tracks that were sufficiently isolated from other tracks. For each plane traversed by a track in this set, the hits from that plane were eliminated from the original hit list used in the track finding. CHEFF then examined the rest of the track to ascertain if it would have been found without the missing plane. If the track would have been found without the missing plane, this plane was clearly redundant for the track in question, and could be used in an efficiency measurement. For each plane, we counted the number of such redundant tracks and the number of redundant tracks in which the original track finding had found a hit in that plane. The quotient of these numbers was taken to be the chamber efficiency. We calculated the chamber efficiency for several intervals of the angle of the track with respect to the chamber normal. Since most of the tracks are rather stiff, the angle cut was also effectively a cut on position in the chamber. No significant trend of efficiency with angle or position was observed. For the Monte Carlo calculation described below, the data were gathered into two angle intervals for each plane. The observed inefficiencies were concentrated near the end of the running period, presumably due to the accumulation of debris on the wires. The track-finding programs would find a track if three out of the possible seven $U$ chambers, two out of the possible six $V$ chambers, and one out of the possible four $W$ chambers had hits. Small-angle tracks traversing all chambers were therefore detected with high efficiency, but large-angle tracks that traversed only three or four chambers were detected with lower efficiency.

We evaluated the geometric acceptance and efficiency for finding tracks in a Monte Carlo calculation. The hadron generators were different for the $\rho^0$, $\omega$, and $\phi$ experiments. The important details of the calculation for each experiment are described in the appropriate individual sections. We generated the events with nonuniform distributions of the hadrons in phase space to take advantage of importance sampling. An appropriate weight was calculated and recorded for each event.

We used the Monte Carlo calculation to correct for the emission of hard photons by the incident and scattered electrons. We allowed the electrons to radiate before and after scattering using the equivalent radiator and peaking approximations.[22] Events with hard photons below 2 GeV were accepted by the kinematic-fit cuts. Above 2 GeV, events were lost in these cuts. The overall correction amounted to about 5%.

Each generated Monte Carlo event was checked to see if its four tracks were in the aperture of the proportional chambers. If so, the locations of its hits in each plane were computed from the reconstruction tables and these hits were randomly deleted according to the measured chamber efficiencies. The positions of the hits that survived the efficiency cuts were smeared to correspond with the measured resolution. To simulate the background hits actually present in real events, we merged the Monte Carlo events with events from "out of time" runs in which the readout system was triggered randomly within the beam spill. The merged hits were then written on tape in the raw data format and these events were passed through the normal analysis chain. The events that survived this process presumably accurately represent the effects of aperture, chamber efficiency, background hits, and reconstruction errors.

The overall efficiency for detecting a $\rho^0$ event in the $Q^2$-$W$ range $1<Q^2<1.3$ GeV$^2$ and $2.3<W<2.9$ GeV with all four charged tracks in the active volume of the chambers was 0.31. This corresponds to an average efficiency of 0.75 for detecting each of the four tracks. The efficiency of 0.31 per event is the product of an efficiency of 0.41 for losses due to chamber inefficiency, and 0.75 for losses due to confusions from background hits in the chambers. The overall efficiency was nearly independent of $Q^2$ and $W$, so it could not introduce a significant spurious $Q^2$ or $W$ dependence in the cross section. We have assigned an overall systematic error of 25% in absolute cross sections due to uncertainties in the efficiency and the number of incident electrons.

## VI. ANALYSIS OF THE $\rho^0$ DATA

### A. $\gamma_V + p \rightarrow \pi^+ + \pi^- + p$ reaction channels

A total of 4637 $e + p \rightarrow e + \pi^+ + \pi^- + p$ candidates with $0.7 < Q^2 < 4$ GeV$^2$ and $1.9 < W < 4$ GeV survived the reconstruction and kinematic fitting described in Sec. IV. These events were divided into the four $Q^2$ bins and three $W$ bins given in Table I.

In our analysis, we assumed that the total $\gamma_V + p \rightarrow \pi^+ + \pi^- + p$ cross section arises from four noninterfering contributions

$$\gamma_V + p \rightarrow \rho^0 + p \ , \qquad (10a)$$

$$\rightarrow \pi^- + \Delta^{++} \ , \qquad (10b)$$

$$\rightarrow \pi^+ + \Delta^0 \ , \qquad (10c)$$

$$\rightarrow \pi^+ + \pi^- + p \ , \qquad (10d)$$

where reaction (10d) is assumed to be $\pi^+\pi^- p$ production with a phase-space (PS) hadron distribution. The total cross section for the $\pi^+\pi^- p$ final state is then given by

$$\sigma(Q^2, W) = \sigma_\rho(Q^2, W) + \sigma_{\Delta^{++}}(Q^2, W) + \sigma_{\Delta^0}(Q^2, W) + \sigma_{\text{PS}}(Q^2, W) \ , \qquad (11)$$

where each contribution can be separated into the longitudinal and transverse terms given in Eq. (4). We separated the terms in Eq. (11) by fitting the differential cross section to the data using the maximum-likelihood (ML) method as described below.

### B. Phenomenology of the $\rho^0$ differential cross section

We assume that the differential cross section for $\rho^0$ electroproduction at fixed $Q^2$ and $W$ can be written in the empirical form

$$\frac{d^5\sigma_\rho}{dm_{\pi\pi}{}^2 dt\, d\Phi\, d\cos\theta\, d\phi} = C_\rho B_\rho(m_{\pi\pi}) S(m_{\pi\pi}) e^{-b_\rho t'} W(\Phi, \cos\theta, \phi) \ . \qquad (12)$$

In this expression, $C_\rho$ is a constant proportional to the cross section, $m_{\pi\pi}$ is the $\pi^+\pi^-$ effective mass, and $B_\rho(m_{\pi\pi})$ is the relativistic $p$-wave Breit-Wigner mass distribution with a mass-dependent width suggested by Jackson,[23]

TABLE I. The $Q^2$ and $W$ limits of the bins used in the $\rho^0$ experiment. Events, $t$ cut refers to the number of events with $0.1 < |t| < 2$ GeV$^2$.

| $W$ (GeV) | $Q^2$ (GeV$^2$) | $\langle W \rangle$ (GeV) | $\langle Q^2 \rangle$ (GeV$^2$) | $\langle \epsilon \rangle$ | Events All $t$ | Events $t$ cut |
|---|---|---|---|---|---|---|
| 1.9–2.3 | 0.7–1.0 | 2.09 | 0.86 | 0.97 | 573 | 548 |
| | 1.0–1.3 | 2.09 | 1.13 | 0.97 | 501 | 460 |
| | 1.3–2.0 | 2.09 | 1.57 | 0.96 | 517 | 422 |
| | 2.0–4.0 | 2.10 | 2.61 | 0.93 | 269 | 186 |
| 2.3–2.9 | 0.7–1.0 | 2.55 | 0.85 | 0.93 | 557 | 488 |
| | 1.0–1.3 | 2.57 | 1.14 | 0.92 | 410 | 371 |
| | 1.3–2.0 | 2.56 | 1.59 | 0.91 | 517 | 453 |
| | 2.0–4.0 | 2.57 | 2.55 | 0.88 | 273 | 218 |
| 2.9–4.0 | 0.7–1.0 | 3.29 | 0.85 | 0.77 | 350 | 283 |
| | 1.0–1.3 | 3.29 | 1.14 | 0.75 | 252 | 220 |
| | 1.3–2.0 | 3.24 | 1.57 | 0.76 | 271 | 234 |
| | 2.0–4.0 | 3.24 | 2.57 | 0.71 | 147 | 132 |
| Total | | | | | 4637 | 4015 |

$$B_\rho(m_{\pi\pi})=\frac{1}{\pi}\frac{m_\rho\Gamma_\rho(m_{\pi\pi})}{(m_{\pi\pi}{}^2-m_\rho{}^2)^2+m_\rho{}^2\Gamma_\rho^2(m_{\pi\pi})} . \tag{13}$$

In this expression, $m_\rho$ is the $\rho^0$ mass and $\Gamma(m_{\pi\pi})$ is the mass-dependent width given by

$$\Gamma_\rho(m_{\pi\pi})=\Gamma_\rho\left[\frac{q_{\pi\pi}}{q_\rho}\right]^3\frac{2q_\rho{}^2}{q_\rho{}^2+q_{\pi\pi}{}^2} , \tag{14}$$

where $\Gamma_\rho$ is the $\rho^0$ width, $q_{\pi\pi}$ momentum of the $\pi^+$ in $\rho^0$ rest frame, and $q_\rho$ is this momentum with $m_{\pi\pi}=m_\rho$.

$S(m_{\pi\pi})$ is an empirical skewing factor similar to that proposed by Ross and Stodolsky,[24]

$$S(m_{\pi\pi})=\left[\frac{m_\rho}{m_{\pi\pi}}\right]^n , \tag{15}$$

where $n$ is a constant to be determined by the data. Photoproduction experiments first demonstrated that some modification of the Breit-Wigner resonance shape was necessary.[6] This effect was explained by Söding[25] as the interference between $\rho^0$ and nonresonant $\pi^+\pi^-$ amplitudes.

The exponential factor represents the forward diffraction peak with the slope parameter $b_\rho$ to be determined from the data. We define $t'$ to be

$$t'=|t-t_{\min}| , \tag{16}$$

where $t$ is the four-momentum transfer to the $\rho^0$, and $t_{\min}$ is its "minimum" value, given by

$$t_{\min}=(E_\gamma^*-E_\rho^*)^2-(p_\gamma^*-p_\rho^*)^2 . \tag{17}$$

Here $E_\gamma^*$ ($E_\rho^*$) and $p_\gamma^*$ ($p_\rho^*$) are the energy and momentum of the virtual photon ($\rho^0$) in the $\gamma_V p$ center-of-mass frame.

$W(\Phi,\cos\theta,\phi)$ describes the angular distribution of the $\pi^+$ and $\pi^-$ in the $\rho^0$ rest frame. We follow the conventions of the DESY Joos[26] experiment, where $\Phi$ is the azimuthal angle of the $\rho^0 p$ production plane around the virtual-photon direction, $\theta$ is the polar angle of the $\pi^+$ in the $\rho^0$ rest frame, and $\phi$ is the azimuthal angle of the $\pi^+$ relative to the plane defined by the virtual photon and the $\rho^0$.[27]

Assuming $s$-channel helicity conservation (SCHC) and natural-parity exchange, $W(\Phi,\cos\theta,\phi)$ can be written as[26,28]

$$\begin{aligned}W(\cos\theta,\psi)=&\frac{3}{8\pi}\frac{1}{1+\epsilon R_\rho}\\&\times\{\sin^2\theta(1+\epsilon\cos2\psi)+2\epsilon R_\rho\cos^2\theta\\&-[2\epsilon(1+\epsilon)R_\rho]^{1/2}\cos\delta\sin2\theta\cos\psi\} ,\end{aligned} \tag{18}$$

where $\psi=\phi-\Phi$. Notice that with these two assumptions, $W(\Phi,\cos\theta,\phi)$ does not depend on $\Phi$ and $\phi$ individually, but only on their differences. In this expression

$$R_\rho=\frac{\sigma_L}{\sigma_T} \tag{19}$$

is the ratio of the longitudinal to the transverse cross section and $\delta$ is the phase difference between the longitudinal and transverse amplitudes.

### C. Phenomenology of the $\Delta^{++}$ and $\Delta^0$ differential cross section

We assumed that the $\Delta^{++}$ production cross section for fixed $Q^2$ and $W$ can be written as

$$\frac{d^2\sigma_{++}}{dm_{++}{}^2dt_{++}}=\frac{C_{++}}{8\pi}\frac{4p_{++}}{W}B_\Delta(m_{++})e^{-b_{++}t'_{++}} , \tag{20}$$

where $m_{++}$ is the $\pi^+p$ effective mass and $t'_{++}=|t_{++}-t_{++\min}|$ ($t_{++}$ is the momentum transfer and $t_{++\min}$ is its minimum value). The factor $4p_{++}/W$, where $p_{++}$ is the momentum of the $\Delta^{++}$ in the hadron center of mass, is a phase-space factor.[15]

The angular distribution of the $p$ and $\pi^+$ in the $\Delta^{++}$ rest system has been found to be nearly isotropic,[15,20] so no angular dependence was included. As before, $B_\Delta(m_{++})$ is the relativistic Breit-Wigner proposed by Jackson,[23]

$$B_\Delta(m_{++})=\frac{1}{\pi}\frac{m_\Delta\Gamma_\Delta(m_{++})}{(m_{++}{}^2-m_\Delta{}^2)^2+m_\Delta{}^2\Gamma_\Delta{}^2(m_{++})} . \tag{21}$$

Here $m_\Delta$ is the $\Delta(1232)$ mass and $\Gamma(m_{++})$ is a mass-dependent width

$$\Gamma_\Delta(m_{++})=\Gamma_\Delta\left[\frac{q_{++}}{q_\Delta}\right]^3\frac{m_\Gamma{}^2+q_\Delta{}^2}{m_\Gamma{}^2+q_{++}{}^2} , \tag{22}$$

and $\Gamma_\Delta$ is the width of the $\Delta(1232)$, $q_{++}$ is the momentum of the $\pi^+$ in the $\Delta^{++}$ rest frame, and $q_\Delta$ is this momentum with $m_{++}=m_\Delta$. $m_\Gamma$ is an empirical parameter which we take[29] to be $m_\Gamma{}^2=2.2m_\pi{}^2$. The exponential factor represents the forward peak in $\Delta^{++}$ production, where the slope parameter $b_{++}$ must also be determined by the fit.

The same expressions were used for $\Delta^0$ production, with $C_0$, $p_0$, $m_0$, $t'_0$, $b_0$, and $q_0$ replacing the corresponding quantities $C_{++}$, $p_{++}$, $m_{++}$, $t'_{++}$, $b_{++}$, and $q_{++}$.

### D. Fitting the data

We determined the cross sections and the other production and decay parameters defined in the previous sections by fitting the data in each $Q^2$-$W$ bin using the method of maximum likelihood. We chose the ML method because it is known to be the most efficient procedure for estimating parameters from data.[30] The usefulness of the ML method in this analysis is evident, since it makes use of each event individually without binning the data. In order to use $\chi^2$ to estimate the above parameters, it would have been necessary to divide the events within a $Q^2$-$W$ bin into bins in the five variables defining the $\pi^+\pi^-p$ final state at fixed $Q^2$ and $W$. This binning would result in substantial loss of information because there would either be few bins, or very few events in most of the bins.

In order to use the ML method, it is necessary to write an explicit expression for the probability density for observing a given event. We started with the yield of $\rho^0$ mesons in one of the $Q^2$-$W$ bins

$$Y_\rho = N_e n_{\rm H} \int \Gamma_W(\vec{v}_\gamma) c_\rho s_\rho(\vec{v}_\gamma) f_\rho(\vec{v}_\rho) \times e(\vec{v}_\gamma,\vec{v}_\rho) d^3\vec{v}_\gamma d^5\vec{v}_\rho \,, \tag{23}$$

where $N_e$ is the number of incident electrons during the live time of the experiment and $n_{\rm H}$ is the number of H atoms per cm$^2$ in the target. We use

$$\vec{v}_\gamma = (Q^2, W, \phi_\gamma) \tag{24}$$

to specify the virtual-photon state and

$$\vec{v}_\rho = (m_{\pi\pi}{}^2, t', \Phi, \cos\theta, \phi) \tag{25}$$

to specify the $\pi^+\pi^-p$ state resulting from $\rho^0$ production and decay. $f_\rho(\vec{v}_\rho)$ is the function defined in Eq. (12),

$$f_\rho(\vec{v}_\rho) = B_\rho(m_{\pi\pi}) S(m_{\pi\pi}) e^{-b_\rho t'} \, W(\Phi, \cos\theta, \phi) \,, \tag{26}$$

and $\Gamma_W(\vec{v}_\gamma)$ was defined in Eq. (7). The function $s_\rho(\vec{v}_\gamma)$ approximates the $Q^2$-$W$ dependence of the $\rho^0$ cross section within a $Q^2$-$W$ bin. The total cross section for producing $\rho^0$ mesons at a given $Q^2$ and $W$ is then related to $c_\rho$ by

$$\sigma_\rho(\vec{v}_\gamma) = c_\rho s_\rho(\vec{v}_\gamma) \int f_\rho(\vec{v}_\rho) d^5\vec{v}_\rho \,. \tag{27}$$

Finally, $e(\vec{v}_\gamma, \vec{v}_\rho)$ is the product of the geometric acceptance and the detection efficiency for the event.[31]

The differential yield is then

$$y_\rho(\vec{v}_\gamma, \vec{v}_\rho) = A_\rho s_\rho(\vec{v}_\gamma) f_\rho(\vec{v}_\rho) \Gamma_W(\vec{v}_\gamma) e(\vec{v}_\gamma, \vec{v}_\rho) \,, \tag{28}$$

where all constants have been absorbed in the parameter $A_\rho$. The total yield will be the sum of four such terms representing $\rho^0$, $\Delta^{++}$, $\Delta^0$, and phase-space contributions. In order to combine these terms into a single probability density, they must be differential in a common set of variables, so it is convenient to replace $\vec{v}_\rho$ by some neutral variables $\vec{v}$ which describe $\pi^+\pi^-p$ phase space. We describe this procedure in Appendix A. The net result is that $f_\rho(\vec{v}_\rho)$ is replaced by a related function $g_\rho(\vec{v})$

$$y_\rho(\vec{v}_\gamma, \vec{v}) = A_\rho s_\rho(\vec{v}_\gamma) g_\rho(\vec{v}) \Gamma_W(\vec{v}_\gamma) e(\vec{v}_\gamma, \vec{v}) \,. \tag{29}$$

The total differential yield summed over all reaction channels becomes

$$\begin{aligned} y(\vec{v}_\gamma, \vec{v}) = [&A_\rho s_\rho(\vec{v}_\gamma) g_\rho(\vec{v}) + A_{++} s_{++}(\vec{v}_\gamma) g_{++}(\vec{v}) \\ &+ A_0 s_0(\vec{v}_\gamma) g_0(\vec{v}) \\ &+ A_{\rm PS} s_{\rm PS}(\vec{v}_\gamma) g_{\rm PS}(\vec{v})] \Gamma_W(\vec{v}_\gamma) e(\vec{v}_\gamma, \vec{v}) \end{aligned} \tag{30a}$$

$$= g(\vec{v}_\gamma, \vec{v}) \Gamma_W(\vec{v}_\gamma) e(\vec{v}_\gamma, \vec{v}) \,. \tag{30b}$$

Note that the functions $e(\vec{v}_\gamma, \vec{v})$ and $\Gamma_W(\vec{v}_\gamma)$ depend only on $\vec{v}_\gamma$ and the $\pi^+\pi^-p$ momentum vectors and do not depend on the specific production and decay channel, so they are common to all four terms.

The probability for observing an event with $(\vec{v}_\gamma, \vec{v})$ is then

$$p(\vec{v}_\gamma, \vec{v} \mid \vec{a}) = \frac{g(\vec{v}_\gamma, \vec{v}) \Gamma_W(\vec{v}_\gamma) e(\vec{v}_\gamma, \vec{v})}{[A_\rho H_\rho + A_{++} H_{++} + A_0 H_0 + A_{\rm PS} H_{\rm PS}]} \tag{31}$$

where

$$H_\rho = \int s_\rho(\vec{v}_\gamma) g_\rho(\vec{v}) \Gamma_W(\vec{v}_\gamma) e(\vec{v}_\gamma, \vec{v}) d^3\vec{v}_\gamma d^5\vec{v} \,. \tag{32}$$

Similar integrals define $H_{++}$, $H_0$, and $H_{\rm PS}$. The vector $\vec{a}$ represents all parameters to be determined by the fit

$$\vec{a} = (A_\rho, b_\rho, R_\rho, \cos\delta, A_{++}, b_{++}, A_0, b_0, A_{\rm PS}) \,. \tag{33}$$

Note that $e(\vec{v}_\gamma,\vec{v})$ appears only as a common factor independent of $\vec{a}$ in the numerator and as a factor in each of the normalization integrals in the denominator. These integrals can be computed as Monte Carlo integrals, using Monte Carlo generated events, without actually calculating $e(\vec{v}_\gamma,\vec{v}_\rho)$. In Appendix B we show that $e(\vec{v}_\gamma,\vec{v})$ disappears from the numerator in the ML fit. Hence, it is not necessary to calculate $e(\vec{v}_\gamma,\vec{v})$ explicitly. Calculating an explicit function essentially requires binning the Monte Carlo events. Hence, many more Monte Carlo events would be required to estimate $e(\vec{v}_\gamma,\vec{v})$ than are necessary to accurately calculate the $H$ integrals, so avoiding the explicit calculation of $e(\vec{v}_\gamma,\vec{v})$ is economical in computer time.

The data in each $Q^2$-$W$ bin were fitted using the probability defined in Eq. (31). For the total-cross-section functions $s_\rho(\vec{v}_\rho)$ and $s_{++}(\vec{v}_{++})$ we used

$$s_\rho(\vec{v}_\gamma)=\frac{1}{(Q^2+m_\rho^2)^2}\ , \tag{34a}$$

$$s_{++}(\vec{v}_\gamma)=\frac{1}{W^3(Q^2+m_\rho^2)^2}\ , \tag{34b}$$

in rough agreement with earlier results.[6,20] For $s_0(\vec{v}_\gamma)$ we used the same function as $s_{++}(\vec{v}_\gamma)$. The fit is insensitive to the precise forms of these functions, so no attempt was made to iterate the fit with better functions determined from the data. The phase-space distribution functions $s_{\rm PS}(\vec{v})$ and $f_{\rm PS}(\vec{v}_{\rm PS})$ were both taken to be 1.

In the fitting we used the Particle Data Group average masses and widths,[32] $m_\rho=776$ MeV, $\Gamma_\rho=158$ MeV, $m_\Delta=1232$ MeV, and $\Gamma_\Delta=115$ MeV, for the masses and widths of the $\rho^0$ and $\Delta(1232)$. The results are insensitive to these parameters, and the data showed no systematic preference for other reasonable values of the masses and widths.

## VII. $\rho^0$ RESULTS

### A. The $\rho^0$ mass distribution and mass skewing

We determined the exponent $n$ in the $\rho^0$ mass skewing factor [Eq. (15)] by fitting the data with $0<|t|<0.7$ GeV$^2$ in each $Q^2$-$W$ bin for the parameters described in Eq. (33) for five different but fixed values of $n$, $n=0,1,2,3,4$. For simplicity, we integrated the $\rho^0$ angular distribution, $W(\cos\theta,\psi)$ over $\psi$ to eliminate the parameter $\delta$ from the fit. The best value of $n$ for each bin was then determined from the resulting likelihood values. The results are presented in Table II and compared with the results of other experiments in Fig. 8. Photoproduction experiments favor values of $n$ near 4, as originally proposed by Ross and Stodolsky,[24] while electroproduction experiments indicate that $n$ decreases with $Q^2$. Our data favor values of $n$ near 1 above $Q^2=0.7$ GeV$^2$.

There is strong evidence that $n$ depends on $t$ in photoproduction and low-$Q^2$ electroproduction experiments.[6] We have also fit the data with a variable $n$ of the form $n(t)=6(1-t/0.6)$ suggested by the photoproduction results. This form leads to poorer fits than fits with constant $n$. We have also fit our data using the skewing factor proposed by Kramer and Quinn,[33]

$$S_{\rm KQ}(m_{\pi\pi},Q^2,t)=\left[\frac{m_\rho{}^2+Q^2+|t|}{m_{\pi\pi}{}^2+Q^2+|t|}\right]^2\ , \tag{35}$$

and found no evidence that this form was preferred by the data.

Since our results are consistent with a constant value of $n$ near 1, we have fixed $n=1$ for the fits used to obtain the rest of the results presented here.

### B. The $\rho^0$, $\Delta^{++}$, $\Delta^0$, and phase-space contributions

With the exponent $n$ in the mass skewing factor fixed at 1, we fitted[34] all data for the parameters $\vec{a}$ given in Eq. (33). In these fits, we restricted the $t$ range to $0.1<|t|<2$ GeV$^2$ to avoid complications due to a possible backward $\rho^0$ peak. Figure 9 shows the $m_{\pi\pi}$ distributions of the data along with distributions determined by the results of the fits. The results are in good agreement with another experiment.[26] The relative contributions of the $\rho^0$,

TABLE II. The empirical Ross-Stodolsky exponent as a function of $Q^2$ and $W$.

| $W$ (GeV) | $Q^2$ (GeV$^2$) | $n$ |
|---|---|---|
| 1.9–2.3 | 0.7–1.0 | 2.35±0.59 |
| | 1.0–1.3 | 0.89±0.74 |
| | 1.3–2.0 | 1.46±0.56 |
| 2.3–2.9 | 0.7–1.0 | 0.48±0.47 |
| | 1.0–1.3 | 0.48±0.54 |
| | 1.3–2.0 | −0.78±0.63 |
| 2.9–4.1 | 0.7–1.0 | 1.29±0.38 |
| | 1.0–1.3 | 0.82±0.63 |
| | 1.3–2.0 | 1.35±0.54 |

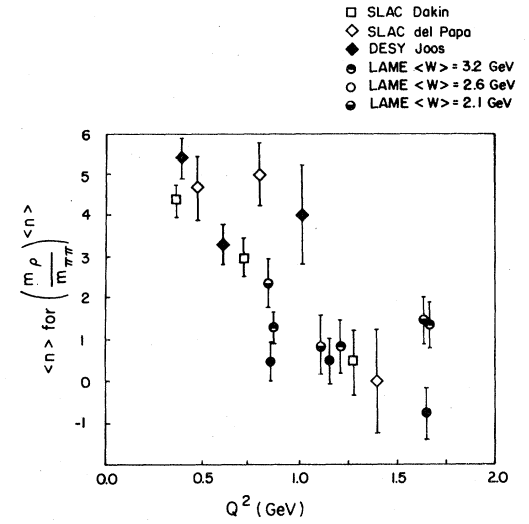

FIG. 8. The best-fit value of the exponent $n$ in the phenomenological Ross-Stodolsky mass-skewing factor plotted versus $Q^2$. Results from other experiments, SLAC Dakin,[41] SLAC del Papa,[44] and DESY Joos,[26] are included.

$\Delta^{++}$, $\Delta^0$, and PS channels are given in Table III. Although the $\Delta^0$ contributions are small, they are generally inconsistent with zero, so we have retained this channel in the fits.

We have also computed cross sections for $\Delta^{++}$ and $\Delta^0$ production using the yields from the fits and the relationship between yield and cross section described in Appendix C. Since these results are in agreement with our previously published $\Delta$ results[20] we do not present them here.

### C. The $\rho^0$ diffractive peak

The width of the forward $\rho^0$ diffraction peak is expected[6,7] to increase as the formation time for the virtual intermediate hadron states in the photon decreases below $c\Delta\tau = 1$ fm. $\Delta\tau$ is the inverse of the energy difference between the virtual photon and the $\rho^0$,

$$\Delta\tau = 1/\Delta E \ , \tag{36}$$

where

$$\Delta E = E_\rho - \nu = (\nu^2 + Q^2 + m_\rho{}^2)^{1/2} - \nu \ , \tag{37}$$

with $E_\rho$ being the energy of the $\rho^0$ in the laboratory system.

In order to exhibit the diffraction peak, we grouped the 12 $Q^2$-$W$ bins into three groups with $\langle c\Delta\tau\rangle = 0.51$, 0.71, and 1.1 fm. In each $\Delta\tau$ bin we divided the data into seven bins of width 0.1 GeV$^2$ in the variable $t' = |t - t_{\min}|$. We then fit the data in each $t'$ bin to a yield of the form[35] given in Eq. (12). With these fits, we computed the longitudinal, transverse, and total cross sections for each $t'$ bin. These cross sections are presented in Table IV. Figure 10 shows the $t'$ distributions and fits. The data are consistent with an exponential $t'$ distribution, in agreement with earlier photo- and electroproduction experiments.[6] These distributions become noticeably flatter as $\langle c\Delta\tau\rangle$ decreases. Each distribution was fit to the form $d\sigma/dt' = Ae^{-bt'}$. The results of the fits are presented in Table V and the values of $b_\rho$ are plotted as functions of $\langle c\Delta\tau\rangle$ in Fig. 11. The longitudinal cross sections have broader diffraction peaks than the transverse cross sections. The diffraction peaks of the longitudinal, transverse, and total cross sections become broader as $\langle c\Delta t\rangle$ decreases.

The overall fits to all of the data with $0.1 < |t| < 2$ GeV$^2$ in the 12 $Q^2$-$W$ bins give more information on the extent to which $b_\rho$ is a function of $Q^2$, $W$, or $\Delta\tau$. Table VI gives the results of these fits for the parameters $b_\rho$, $R_\rho$, and $\cos\delta$ for each of the 12 $Q^2$-$W$ bins. The $b_\rho$ values are plotted versus $Q^2$ and $W$ in Figs. 12 and 13, respectively. $b_\rho$ does not appear to be a single function of either $Q^2$ or $W$ alone; in each graph the data tend to lie on families of curves. Figure 14 shows the same data plotted versus $c\Delta\tau$, along with the results of several photoproduction[36–40] and some other electroproduction[26,41–44] experiments. The electroproduction experiments chosen are all ones in which two or three hadrons are detected (1C and 4C experiments). Our data show that $b_\rho$ is primarily a function of $\Delta\tau$, although we cannot rule out some residual dependence on $Q^2$ or $W$. Our $b_\rho$ results lie on a smooth curve that increases with $\Delta\tau$ towards values near 7 or 8 GeV$^{-2}$ which are favored by the higher-energy photoproduction data. Our data appear to be inconsistent with the DESY Joos[26] electroproduction experiment, but to agree with the ABBHM[36] photoproduction experment, at similar values of $\Delta\tau$. Figure 15 shows that our data agree well with those of an earlier Cornell missing-mass experiment[45] in which only the scattered electron and proton were detected.

We conclude that the width of the $\rho^0$ diffraction peak increases dramatically as the formation time of the virtual hadron states in the photon decreases below $c\Delta\tau = 1$ fm. Since our data are all at low values of $c\Delta\tau$, we would not be able to observe the increase in the width of the diffraction peak with

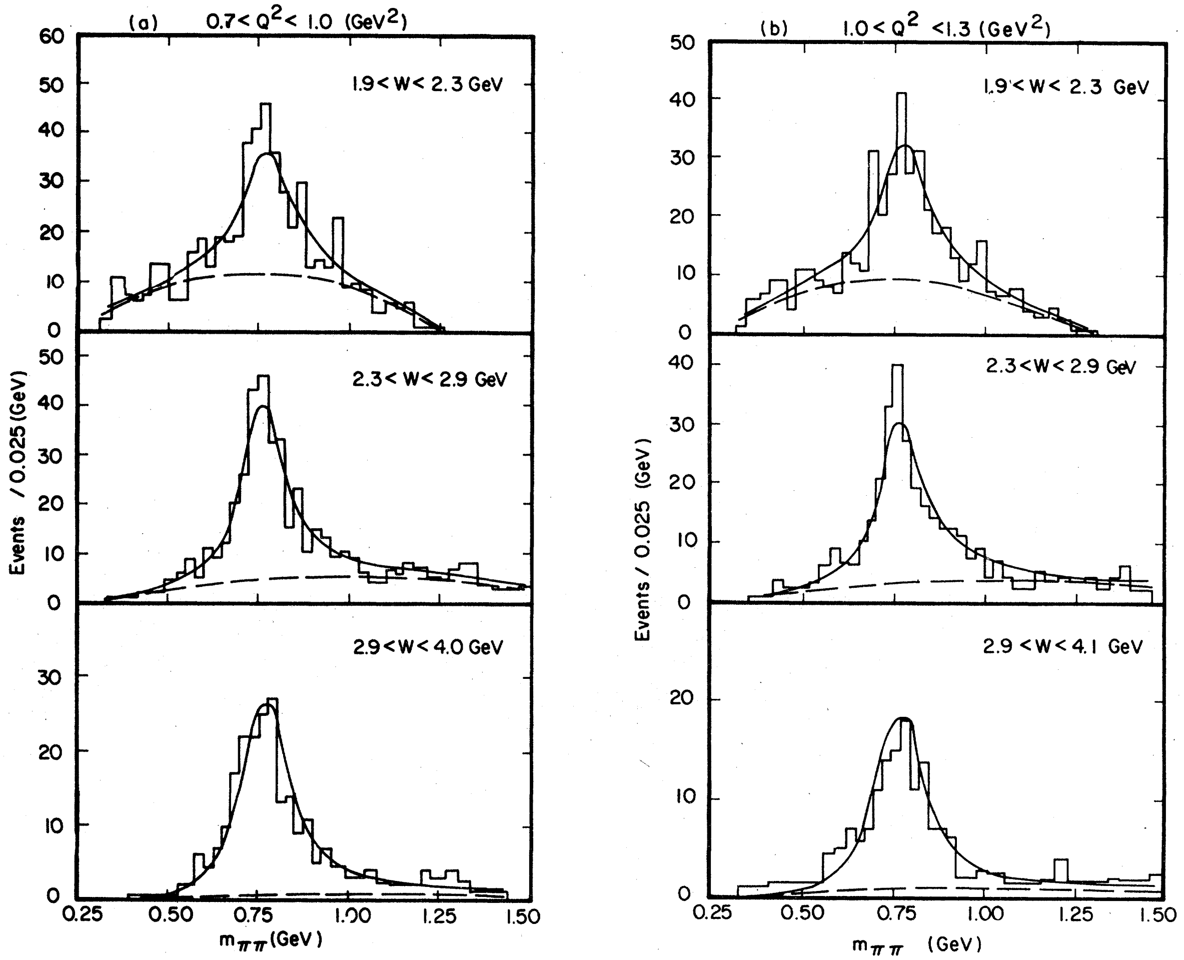

FIG. 9. The $m_{\pi\pi}$ distributions for all 12 $Q^2$-$W$ bins. The solid curves are the fits to the total mass distribution; the dashed curves are the $\Delta^{++}$, $\Delta^0$, and phase-space contributions determined by the fits.

increasing $Q^2$ that is expected to occur at large $\Delta_T$.[46,47]

### D. $R_\rho=\sigma_L/\sigma_T$ and the phase $\delta$

The most general angular distribution for $\rho^0$ decay is given in terms of 15 measurable density-matrix elements.[28,26] Measuring these matrix elements using the ML fit would require introducing an intolerable additional 13 parameters above those given in Eq. (33) into the fit. Joos *et al.*[26] have avoided this difficulty by using the method of moments to extract these matrix elements from the data. Although our angular acceptance is sufficiently flat for the fits presented here, we did not feel confident that the method of moments would reliably determine all of the density matrix elements in our experiment since the acceptance is less than $4\pi$. Figure 16 shows the acceptance of our detector as a function of $\psi$. The relative acceptance is approximately given by $a(\psi)=0.8+0.2\cos 2\psi$. Since we take the acceptance into account as described earlier, it causes no problems[48] with the ML fits. However, this acceptance would invalidate a moment calculation done without weighting the events, because the individual terms in the density matrix would no longer be orthogonal. We chose instead to assume that SCHC and natural-parity-exchange amplitudes dominate $\rho^0$ electroproduction in accord with the results of Joos *et al.*[26] This assumption reduces[28,26] the angular distribution to the form given in Eq. (18) with only two parameters $R_\rho$ and $\delta$ to be determined from the data.

Our angular distributions for $\cos\theta$ and $\psi$, together with the results of the fit are shown in Figs. 17 and 18, respectively. The fits are in excellent

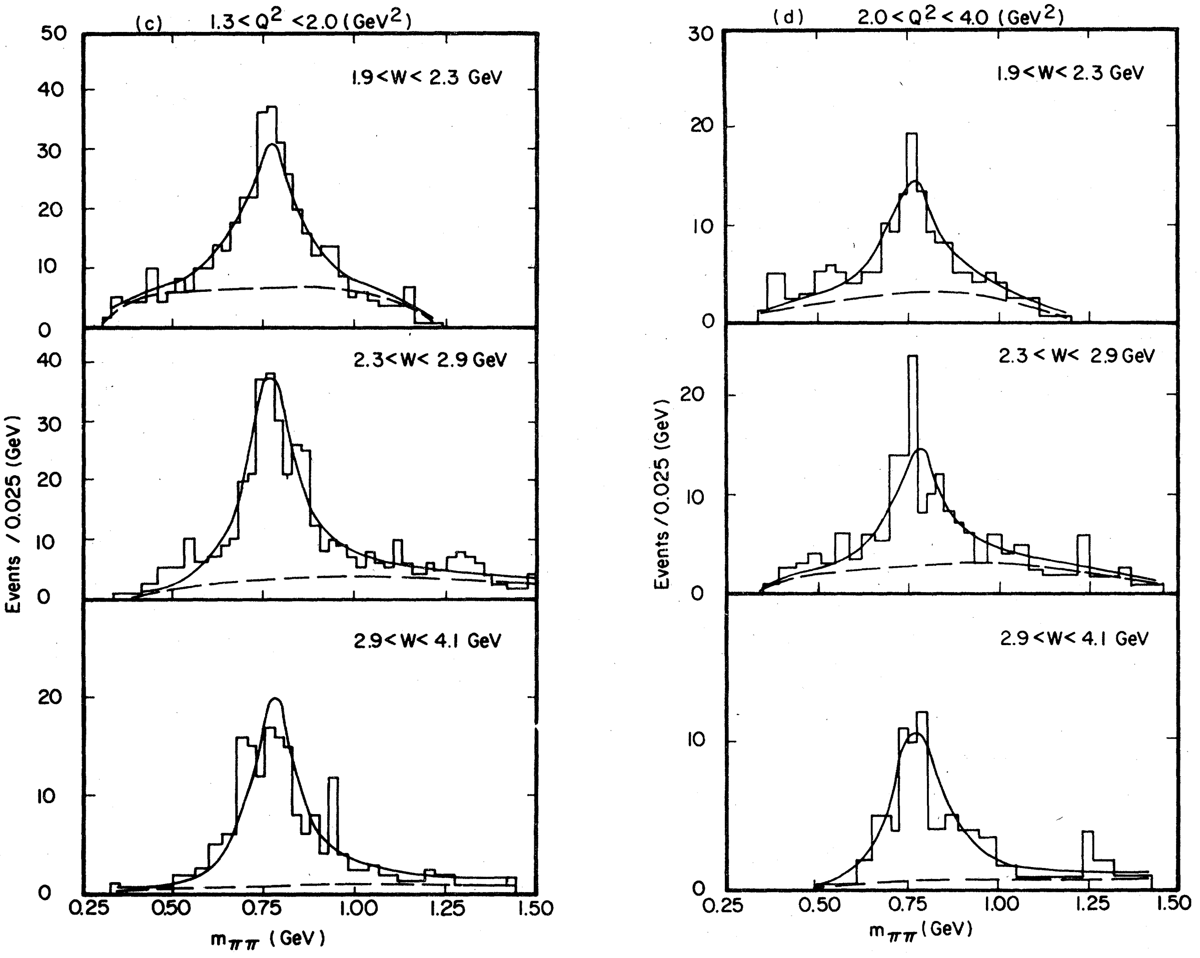

FIG. 9. *(Continued).*

TABLE III. Relative cross sections in percent for $\rho$, $\Delta^{++}$, $\Delta^0$, and phase-space electroproduction and the total $\gamma_V + p \rightarrow \pi^+ + \pi^- + p$ cross section.

| $W$ (GeV) | $Q^2$ (GeV$^2$) | $\rho$ | $\Delta^{++}$ | $\sigma^0$ | PS | $\sigma_{\text{tot}}$ |
|---|---|---|---|---|---|---|
| 1.9−2.3 | 0.7−1.0 | 29±3 | 26±3 | 7±2 | 38± 5 | 18.7±1.3 |
| | 1.0−1.3 | 33±4 | 12±2 | 3±1 | 52± 6 | 6.8±0.5 |
| | 1.3−2.0 | 36±4 | 15±3 | 2±1 | 46± 7 | 3.8±0.3 |
| | 2.0−4.0 | 32±5 | 12±3 | 2±2 | 55±13 | 1.8±0.3 |
| 2.3−2.9 | 0.7−1.0 | 43±3 | 22±3 | 8±2 | 27± 4 | 6.4±0.4 |
| | 1.0−1.3 | 42±4 | 16±3 | 7±2 | 35± 7 | 3.1±0.3 |
| | 1.3−2.0 | 40±3 | 4±2 | 4±1 | 52± 7 | 2.0±0.2 |
| | 2.0−4.0 | 20±3 | 16±3 | 8±3 | 57±13 | 1.1±0.1 |
| 2.9−4.1 | 0.7−1.0 | 69±5 | 11±3 | 5±2 | 14± 5 | 1.5±0.1 |
| | 1.0−1.3 | 77±7 | 33±6 | 11±3 | −21±12 | 0.8±0.1 |
| | 1.3−2.0 | 49±4 | 21±4 | 5±2 | 25±11 | 0.7±0.1 |
| | 2.0−4.0 | 47±6 | 16±4 | 10±4 | 27±27 | 0.4±0.1 |

TABLE IV. Differential $\rho^0$ cross sections.

| $\langle c\Delta\tau\rangle$ (fm) | $t'$ (GeV$^2$) | $d\sigma_\rho/dt'$ ($\mu$b/GeV$^2$) | $d\sigma_L/dt'$ ($\mu$b/GeV$^2$) | $d\sigma_T/dt'$ ($\mu$b/GeV$^2$) |
|---|---|---|---|---|
| 0.51 | 0.1–0.2 | $0.443\pm0.059$ | $0.223\pm0.053$ | $0.235\pm0.051$ |
| | 0.2–0.3 | $0.432\pm0.066$ | $0.234\pm0.060$ | $0.215\pm0.055$ |
| | 0.3–0.4 | $0.352\pm0.061$ | $0.185\pm0.055$ | $0.179\pm0.052$ |
| | 0.4–0.5 | $0.148\pm0.036$ | $0.083\pm0.040$ | $0.071\pm0.036$ |
| | 0.5–0.6 | $0.297\pm0.058$ | $0.159\pm0.050$ | $0.150\pm0.047$ |
| | 0.6–0.7 | $0.260\pm0.072$ | $0.260\pm0.074$ | $0.018\pm0.018$ |
| | 0.7–0.9 | $0.248\pm0.045$ | $0.202\pm0.044$ | $0.061\pm0.026$ |
| 0.71 | 0.1–0.2 | $1.239\pm0.083$ | $0.743\pm0.082$ | $0.550\pm0.070$ |
| | 0.2–0.3 | $0.928\pm0.080$ | $0.549\pm0.076$ | $0.418\pm0.066$ |
| | 0.3–0.4 | $0.367\pm0.047$ | $0.172\pm0.042$ | $0.207\pm0.043$ |
| | 0.4–0.5 | $0.429\pm0.055$ | $0.226\pm0.051$ | $0.219\pm0.048$ |
| | 0.5–0.6 | $0.258\pm0.050$ | $0.169\pm0.045$ | $0.101\pm0.035$ |
| | 0.6–0.7 | $0.284\pm0.052$ | $0.163\pm0.047$ | $0.132\pm0.041$ |
| | 0.7–0.9 | $0.176\pm0.032$ | $0.167\pm0.035$ | $0.022\pm0.017$ |
| 1.1 | 0.1–0.2 | $1.634\pm0.105$ | $0.670\pm0.116$ | $1.079\pm0.118$ |
| | 0.2–0.3 | $1.075\pm0.087$ | $0.365\pm0.106$ | $0.773\pm0.107$ |
| | 0.3–0.4 | $0.598\pm0.069$ | $0.288\pm0.076$ | $0.359\pm0.071$ |
| | 0.4–0.5 | $0.398\pm0.059$ | $0.131\pm0.063$ | $0.289\pm0.066$ |
| | 0.5–0.6 | $0.416\pm0.064$ | $0.317\pm0.079$ | $0.153\pm0.055$ |
| | 0.6–0.7 | $0.178\pm0.086$ | $0.045\pm0.037$ | $0.140\pm0.072$ |
| | 0.7–0.9 | $0.092\pm0.024$ | $0.099\pm0.029$ | $0.010\pm0.009$ |

agreement with the data, which supports our assumption that SCHC and natural-parity exchange are consistent with our data.

The values of $R_\rho$ and $\cos\delta$ obtained from the fits are included in Table VI. There is no consistent trend in $R_\rho$ with $W$, so we averaged the three $R_\rho$ values at a given $Q^2$ before plotting them in Fig. 19. The results of two earlier experiments[42,26] suggested that $R_\rho$ increases linearly with $Q^2$ according to

$$R_\rho=\xi^2\frac{Q^2}{m_\rho{}^2} \tag{38}$$

with $0.3<\xi^2<0.5$. Our results show that $R_\rho(Q^2)$ deviates markedly from this linear dependence on $Q^2$ for $Q^2>1$ GeV$^2$, in agreement with two other experiments.[43,44]

The cosine of the phase $\delta$ between the longitudinal and transverse amplitudes is shown in Fig. 20. $\cos\delta$ appears to be independent of $Q^2$, so we have averaged over $Q^2$ before plotting it as a function of $W$. Our measured values of $\cos\delta$ increase with $W$ in agreement with the trends of other experiments, but our results are significantly lower than those of the DESY Joos[26] experiment at lower $Q^2$. It is difficult to ascribe this discrepancy to an error in our acceptance, since $\cos\delta$ multiplies $\cos\psi$ in the $\rho^0$ distribution [Eq. (18)] and the acceptance (see Fig. 16) is essentially independent of $\cos\psi$.

### E. The $\rho^0$ total cross section

We obtained the $\rho^0$ cross section $\sigma_\rho(Q^2,W)$ from the fit parameter $A_\rho$ using the prescription in Appendix C. The results appear in Table VII and Fig. 21. Our data obviously depend on $W$ as well as $Q^2$. As discussed in Sec. V, we estimate a systematic error of ±25% in the normalization in addition to the statistical errors quoted in the table.

Since this $W$ dependence was not immediately apparent in previous experiments, it is difficult to compare our results directly with them. In order to facilitate comparison, we choose to compare each experiment with a diffractive vector-meson-dominance prediction for the cross section[6,26,49]

$$\sigma_{\text{dif}}(Q^2,W)=\frac{\sigma_\rho(0,W)}{(1+Q^2/m_\rho{}^2)^2}\,\frac{p_\gamma^*(0)}{p_\gamma^*(Q^2)}\times(1+\epsilon R_\rho)e^{-b_\rho|t_{\min}(Q^2)-t_{\min}(0)|}\ . \tag{39}$$

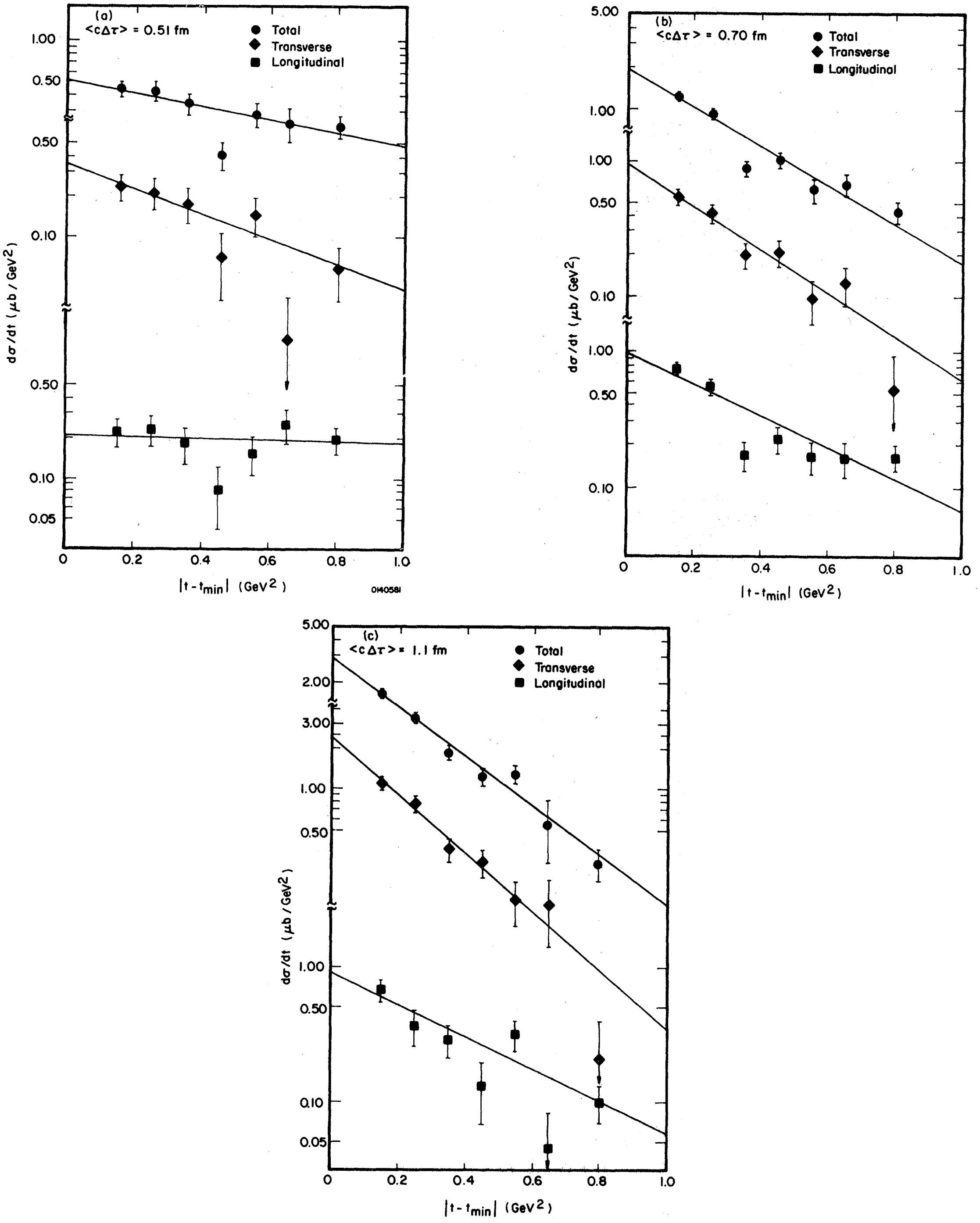

FIG. 10. $d\sigma_\rho/dt'$ plotted against $t' = |t - t_{\min}|$ for three intervals of $\langle c\Delta\tau\rangle$. The straight lines are the fits to the form $d\sigma_\rho/dt' = Ae^{-b_\rho t'}$.

The factor $\sigma_\rho(0,W)/(1+Q^2/m_\rho{}^2)^2$ represents the photoproduction cross section extrapolated to $Q^2$ by the square of the $\rho^0$ propagator. The $(1+\epsilon R_\rho)$ factor corrects this cross section for the longitudinal component which is missing at $Q^2=0$. The exponential factor corrects for the fact that a given $W$ the physical $t$ range is smaller when $Q^2>0$ than it is at $Q^2=0$. The factor $p_\gamma^*(0)/p_\gamma^*(Q^2)$, where

TABLE V. Results of the fits of the differential $\rho^0$ cross sections to the form $d\sigma/dt'=Ae^{-bt'}$. $\sigma_\rho$, $\sigma_L$, and $\sigma_T$ refer to the total, longitudinal, and transverse cross sections, respectively. There were five degrees of freedom in each fit.

| $\langle c\Delta\tau\rangle$ (fm) | | $A$ ($\mu$b/GeV$^2$) | $b_\rho$ (GeV$^{-2}$) | $\chi^2$ |
|---|---|---|---|---|
| 0.51 | $\sigma_\rho$ | $0.50\pm0.07$ | $1.04\pm0.30$ | 10.8 |
| | $\sigma_L$ | $0.21\pm0.05$ | $0.09\pm0.43$ | 5.3 |
| | $\sigma_T$ | $0.34\pm0.08$ | $2.09\pm0.62$ | 5.2 |
| 0.71 | $\sigma_\rho$ | $1.91\pm0.15$ | $3.26\pm0.22$ | 21.9 |
| | $\sigma_L$ | $0.99\pm0.12$ | $2.71\pm0.31$ | 17.9 |
| | $\sigma_T$ | $0.94\pm0.16$ | $3.57\pm0.49$ | 5.6 |
| 1.1 | $\sigma_\rho$ | $3.01\pm0.26$ | $4.19\pm0.27$ | 7.6 |
| | $\sigma_L$ | $0.91\pm0.18$ | $2.74\pm0.47$ | 9.3 |
| | $\sigma_T$ | $2.37\pm0.37$ | $4.95\pm0.53$ | 5.1 |

$p_\gamma^*(Q^2)$ is the virtual-photon momentum in the $\gamma_V p$ center of mass, represents a correction to the virtual-photon flux.[49] This factor is one measure of the ambiguity[6] in the prediction; it arises from a choice made in the definition of the transverse-photon flux[11] in Eq. (2).

For $\sigma_\rho(0,W)$ we have used the expression suggested by Wolf,[50]

$$\sigma_\rho(0,W)=A_\gamma/E_\gamma+B_\gamma\ , \tag{40}$$

where $E_\gamma$ is the proton energy. A fit to available protoproduction data yielded $A_\gamma=29.4\pm2.5$ $\mu$b GeV and $B_\gamma=9.5\pm0.5$ $\mu$b. $A_\gamma$ and $B_\gamma$ are strongly correlated, $\langle\delta A\delta B\rangle/(\sigma_A\sigma_B)=-0.87$. In Fig. 22 we show the data and the fit.

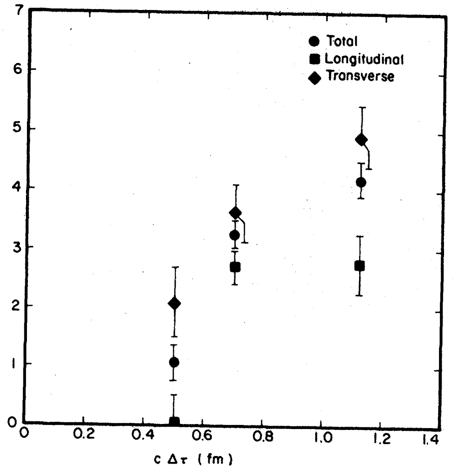

FIG. 11. The $\rho^0$ slope parameter $b_\rho$ for longitudinal, transverse, and total cross sections from the fits to the data in the preceeding figure, plotted versus $c\Delta\tau$.

We have used our experimental values of $b_\rho$ and $R_\rho$ in computing the model predictions.[51] In Fig. 23 we exhibit the ratio $\sigma_\rho(Q^2,W)/\sigma_{\rm dif}(Q^2,W)$ for our experiment. At fixed $W$, the ratio is nearly independent of $Q^2$, except for a possible increase at higher and lower $Q^2$. However, the data still fall on distinct curves for the three different values of $W$. The $W$ dependence of $\sigma_{\rm dif}(Q^2,W)$ explicitly introduced through $\sigma_\rho(0,W)$ and implicitly introduced in the rest of the expression is not sufficient to explain the $W$ dependence of $\sigma_\rho(Q^2,W)$ in Fig. 21. Although these ratios are nearly independent of $Q^2$, a small-term quadratic in $Q^2$ would also be consistent with the data.

We have previously reported[1] this $W$ dependence in an earlier analysis of a smaller sample of our data. In the meantime we have not only increased the size of the data sample, but we have made substantial improvements in the quality of the reconstruction and the kinematic selection of $e+p\to e+\pi^++\pi^-+p$ candidates. We have also replaced an older, less exact, $\chi^2$ fit with the new ML fit described here and we have improved the Monte Carlo calculation of acceptance and efficiency as outlined in this paper. Because of our observed $W$ dependence, we have paid particular attention to $W$-dependent factors and possible sources of systematic error in the $W$ dependence. We were not able to find errors that could account for this effect.

It is interesting to examine data from other experiments to see if they are consistent with our trend. Figure 24 shows $\sigma_\rho(Q^2,W)/\sigma_{\rm dif}(Q^2,W)$ for several other electroproduction experiments.

TABLE VI. $b_\rho$, $R_\rho$, and cosδ for $\rho^0$ electroproduction as functions of $W$ and $Q^2$.

| $W$ (GeV) | $Q^2$ (GeV$^2$) | $b_\rho$ (GeV$^{-2}$) | $R_\rho$ | cosδ |
|---|---|---|---|---|
| 1.9−2.3 | 0.7−1.0 | 2.01±0.35 | 1.25±0.35 | −0.10±0.13 |
| | 1.0−1.3 | 2.07±0.32 | 1.14±0.31 | −0.35±0.13 |
| | 1.3−2.0 | 1.71±0.25 | 1.41±0.37 | −0.30±0.12 |
| | 2.0−4.0 | 1.15±0.38 | 1.67±0.67 | −0.23±0.18 |
| 2.3−2.9 | 0.7−1.0 | 4.15±0.36 | 0.47±0.13 | 0.37±0.11 |
| | 1.0−1.3 | 3.77±0.47 | 1.11±0.26 | 0.23±0.12 |
| | 1.3−2.0 | 3.03±0.29 | 0.86±0.19 | −0.04±0.09 |
| | 2.0−4.0 | 2.45±0.57 | 0.38±0.20 | 0.05±0.24 |
| 2.9−4.1 | 0.7−1.0 | 5.21±0.40 | 0.46±0.15 | 0.67±0.13 |
| | 1.0−1.3 | 3.96±0.35 | 1.12±0.31 | 0.38±0.13 |
| | 1.3−2.0 | 3.55±0.39 | 1.25±0.36 | 0.50±0.12 |
| | 2.0−4.0 | 2.54±0.40 | 1.42±0.46 | −0.11±0.19 |

Again, we have used values of $b_\rho$ and $R_\rho$ from the experiments themselves to calculate $\sigma_{\rm dif}(Q^2,W)$. Only the DESY Joos[26] and the SLAC del Papa[44] experiments offer cross-section measurements over a range of $W$ values near ours. Although the errors here are larger than in our experiment, the same tendency for $\sigma_\rho(Q^2,W)/\sigma_{\rm dif}(Q^2,W)$ to decrease as $W$ increases appears to be present.

Figure 25 illustrates $\sigma_\rho/\sigma_{\rm dif}$ averaged over $Q^2$ and plotted versus $W$. In our relatively precise data, a decrease in this ratio with $W$ is evident. The other experiments with data at several $W$ values in our $W$ region exhibit the same trend within their experimental errors. The differences in normalization among experiments are consistent with the quoted overall systematic errors and the possible residual $Q^2$ dependence in our data.

## VIII. ω ANALYSIS AND RESULTS

### A. Previous results and expectations for ω electroproduction

The diffractive vector-meson-dominance prediction for ω electroproduction [Fig. 1(b)] is given by Eq. (39).

$$\sigma_{\omega\,\rm dif}(Q^2,W)=\frac{\sigma_\omega(0,W)}{(1+Q^2/m_\omega{}^2)^2}\frac{p_\gamma^*(0)}{p_\gamma^*(Q^2)}\times(1+\epsilon R_\omega)e^{-b_\omega|t_{\rm min}(Q^2)-t_{\rm min}(0)|}\ . \tag{41}$$

According to this model, the $\omega/\rho^0$ ratio would then be

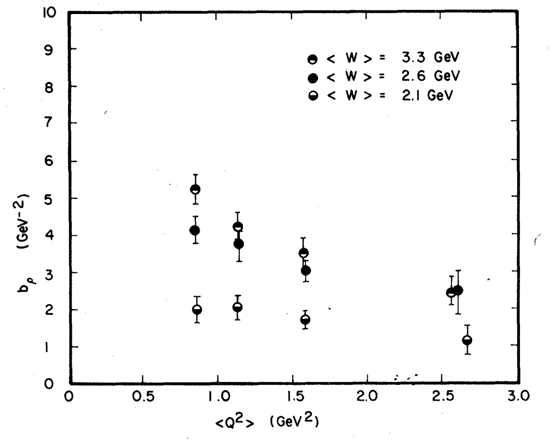

FIG. 12. The $\rho^0$ slope parameters found in this experiment plotted versus $Q^2$.

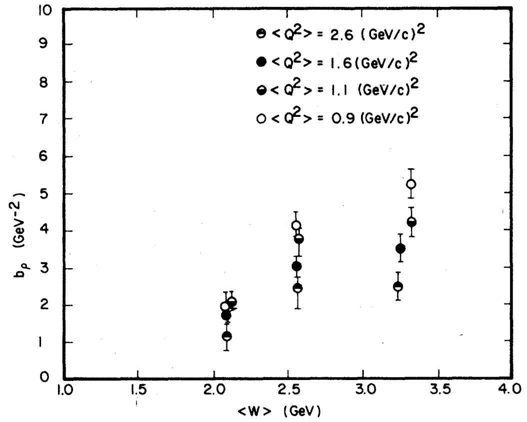

FIG. 13. The $\rho^0$ slope parameters found in this experiment plotted versus $W$.

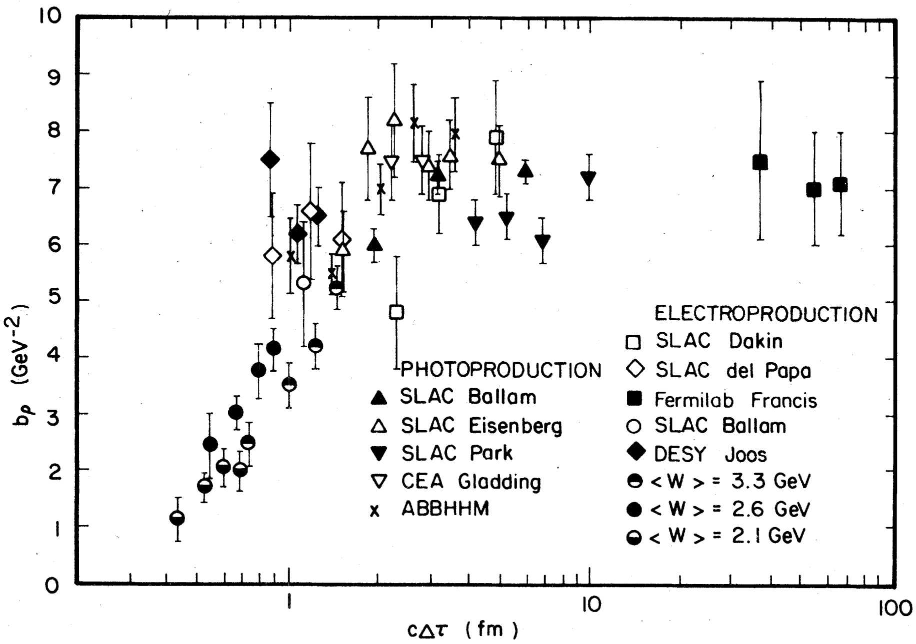

FIG. 14. The $\rho^0$ slope parameters found in this experiment plotted versus $c\Delta\tau$, along with results from the photoproduction experiments SLAC Ballam,[38] SLAC Eisenberg,[37] SLAC Park,[38] CEA Gladding,[40] and ABBHM[36] and the electroproduction experiments, Fermilab Francis,[43] SLAC Dakin,[44] SLAC del Papa,[44] SLAC Bellam,[42] and DESY Joos.[26]

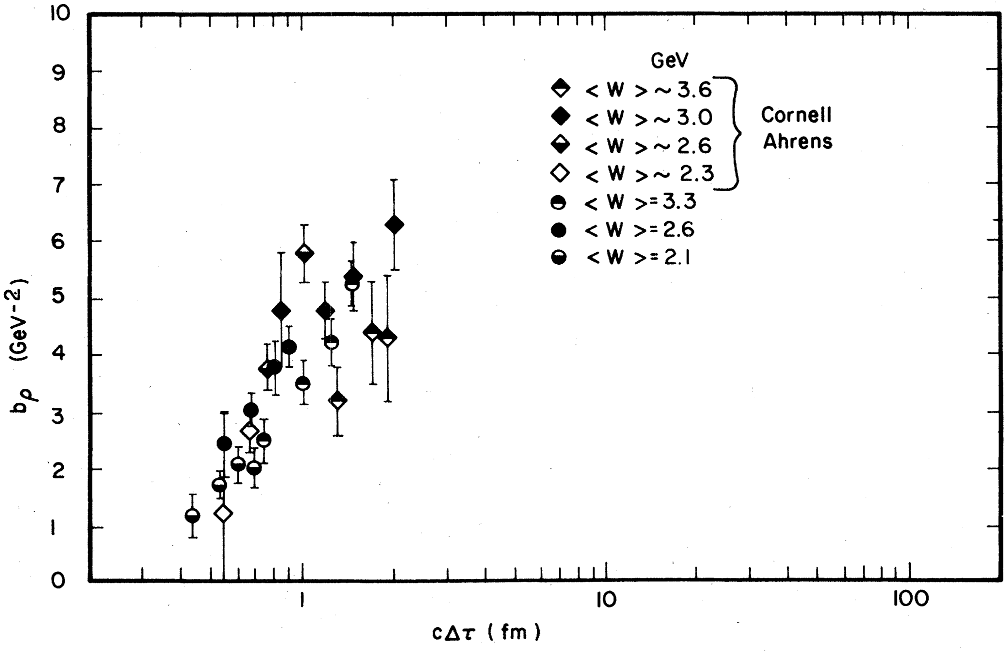

FIG. 15. The $\rho^0$ slope parameters found in this experiment plotted versus $c\Delta\tau$, along with results from the Cornell Ahrens electroproduction experiment.[45]

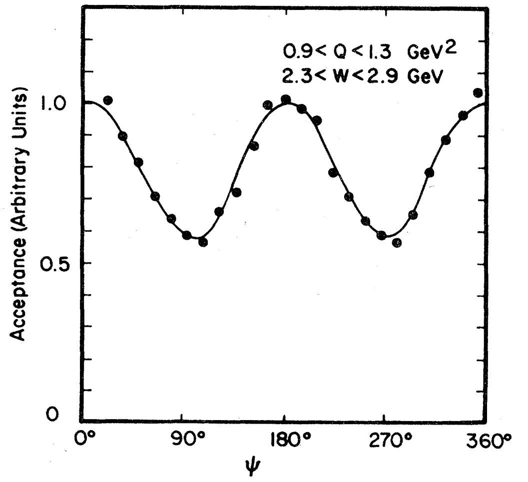

FIG. 16. The acceptance of our detector as a function of $\psi$ for $\rho^0$ events with $0.9 < Q^2 < 1.3$ GeV$^2$ and $2.3 < W < 2.9$ GeV. The scatter in the dots illustrates the statistical fluctuations in the Monte Carlo acceptance calculation.

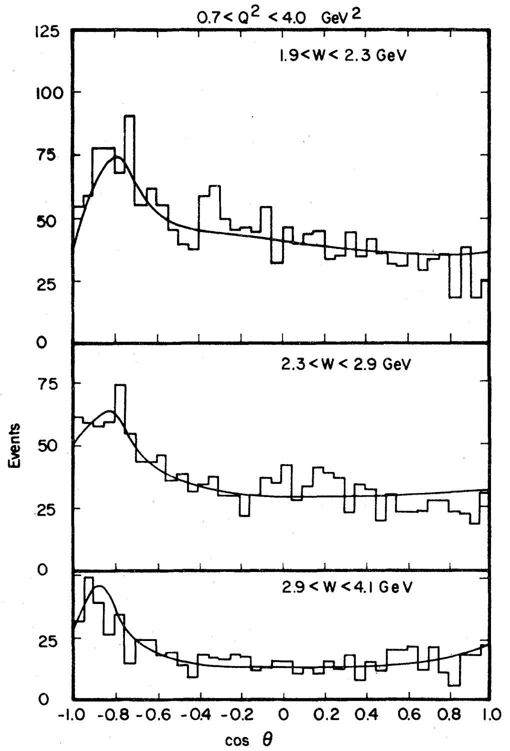

FIG. 17. The $\cos\theta$ distributions for $\rho^0$ electroproduction in three $W$ intervals. The curve is the fit to the data. The peak near $\cos\theta = -1$ is due to the $\Delta$ contributions.

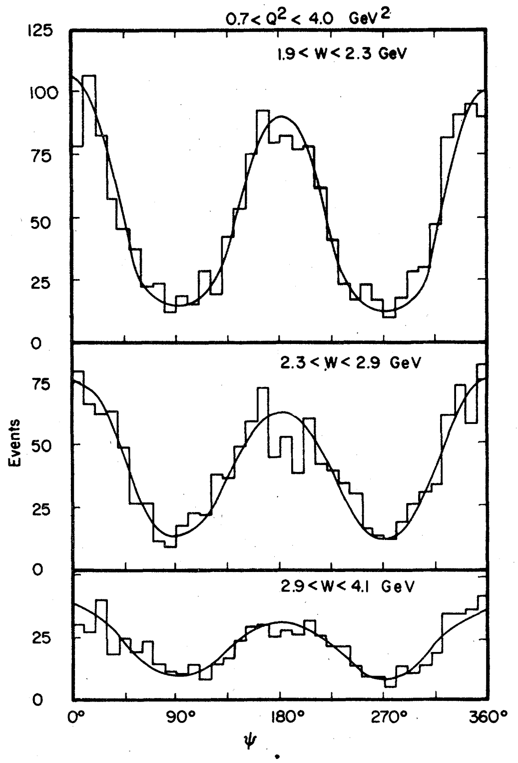

FIG. 18. The $\psi$ distributions and fits for three $W$ intervals.

$$\frac{\sigma_{\omega\,\mathrm{dif}}(Q^2,W)}{\sigma_{\rho\,\mathrm{dif}}(Q^2,W)} = \frac{\sigma_\omega(0,W)}{\sigma_\rho(0,W)} \frac{(1+Q^2/m_\rho^2)^2}{(1+Q^2/m_\omega^2)^2} \frac{(1+\epsilon R_\omega)}{(1+\epsilon R_\rho)} \times e^{-(b_\omega-b_\rho)|t_{\min}(Q^2)-t_{\min}(0)|} . \qquad (42)$$

This ratio is essentially independent of $Q^2$, since $m_\omega \simeq m_\rho$, $\epsilon$ is nearly constant over the $Q^2$-$W$ range of this experiment (Table I) and $b_\omega$ is not far from $b_\rho$ (Sec. VIII D).

In addition to the diffractive VMD contribution, the one-pion-exchange (OPE) VMD diagram in Fig. 26 is important. The importance of this diagram is due to the quark-model suppression of the $\gamma\omega$ vertex[6] relative to the $\gamma\rho$ vertex. This OPE contribution is necessary to fit lower-energy $\omega$ photoproduction data.[36,38] Fraas[52] and Joos *et al*[53] have extended this OPE model to electroproduction. Joos *et al.* find that the diffractive and OPE contributions describe their $\omega$ electroproduction data quite well for $W > 2$ GeV, where we have data. Below $W = 2$ GeV they need an additional contribution, presumably $s$ channel. Near $W = 2$ GeV the OPE contribution is expected to be larger

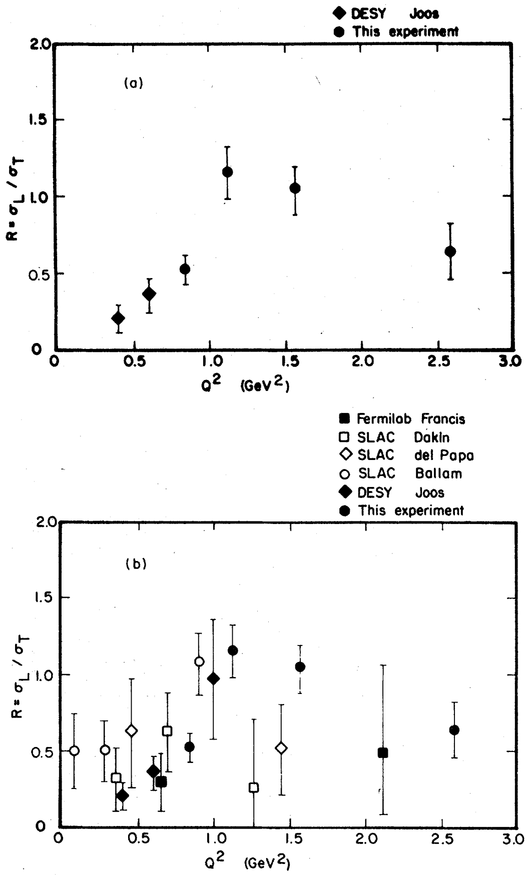

FIG. 19. The longitudinal-transverse ratio $R_\rho$ plotted versus $Q^2$. The results of this experiment have been averaged over $W$. In (a) results from the DESY Joos[26] experiment are also included, but results with larger errors are arbitrarily excluded. In (b) we also include results from the Fermilab Francis,[43] SLAC Dakin,[41] SLAC del Papa,[44] SLAC Bellam,[42] and DESY Joos[26] experiments.

than diffraction, but diffraction is expected to dominate above $W=2.5$ GeV. In any event, the $Q^2$ dependence of the OPE contribution is dominated by the square of the $\rho^0$ propagator, so the $\omega/\rho^0$ ratio should still be independent of $Q^2$, regardless of the OPE-to-diffraction ratio. The results of the DESY Joos[53] and SLAC Ballam[42] electroproduction experiments agree with this prediction.

### B. Selection of $e+p\to e+\pi^+ +\pi^- +\pi^0+p$ events

As mentioned in Sec. IV, the photons from $\pi^0$ decay were not observed, so $\omega$ electroproduction events appeared as 1C events in this experiment. The loss of three constraints, compared to $\rho^0$ or $\phi$ electroproduction, resulted in larger backgrounds, so more effort was required to select $\omega$ events.[4] This analysis was restricted to events obtained in the first 40% of the data run.

Ignoring $K$-meson production, three 1C combinations had to be considered, one in which the missing neutral was a neutron, and two (due to the $p$-$\pi^+$ ambiguity) in which the missing neutral was a $\pi^0$. If $K$-meson hypotheses had been allowed, there would have been eight additional baryon-number- and strangeness-conserving combinations. We ignored these $K$ hypotheses to avoid the large combinatorial background. We feel certain that this assumption is reasonable, since (a) the $K/\pi$ ratio is small in our own 4C events and in studies of inclusive $\pi$ and $K$ yields in electroproduction[54] and (b) the $\omega$ is narrow, so any resultant background due to $K$ production should contribute to the broad background instead of the $\omega$ peak.

We first defined our $\pi^+\pi^-\pi^0$ sample as those events for which one of the two $\pi^0$ hypotheses gave the lowest 1C kinematic $\chi^2$. For these events, a peak in the $\pi^+\pi^-\pi^0$ effective mass ($m_{3\pi}$) distribution at the $\omega$ mass[32] ($m_\omega=783$ MeV) was clearly visible above a large background.

We next used the time-of-flight (TOF) counters to improve the identification of the positive particles. Approximately 40% of the positive particles hit one of the TOF banks. Using the measured time of flight and the momentum, we calculated $\chi^2$ values for the $\pi^+$ and $p$ identification hypotheses. We then used the sum of the kinematic and the TOF $\chi^2$ values to select the most likely of the three combinations. This refinement resulted in an enhancement of the $\omega$ signal. The resulting $m_{3\pi}$ distribution is shown in Fig. 27.

These particle assignments were retained throughout the following cuts used to define the final data sample: (a) We rejected events with a 4C $\chi^2<40$ if the 4C hypothesis was consistent with the TOF and Čerenkov-counter information as described in (d) and (e) below. (b) We rejected events in which the 1C $\chi^2$ was greater than 10. (c) Since the kinematic fit is nonlinear and was calculated by successive approximations, the fit did not always converge to an energy-conserving solution. We rejected events in which the error in energy conservation was greater than 1 MeV. (d) We rejected events in our sample with large TOF $\chi^2$ for the hypothesis with smallest total $\chi^2$ if there was a different hypothesis with a sufficiently small TOF $\chi^2$. (e) We rejected events if the particle identified as a proton was below the proton Čerenkov thresh-

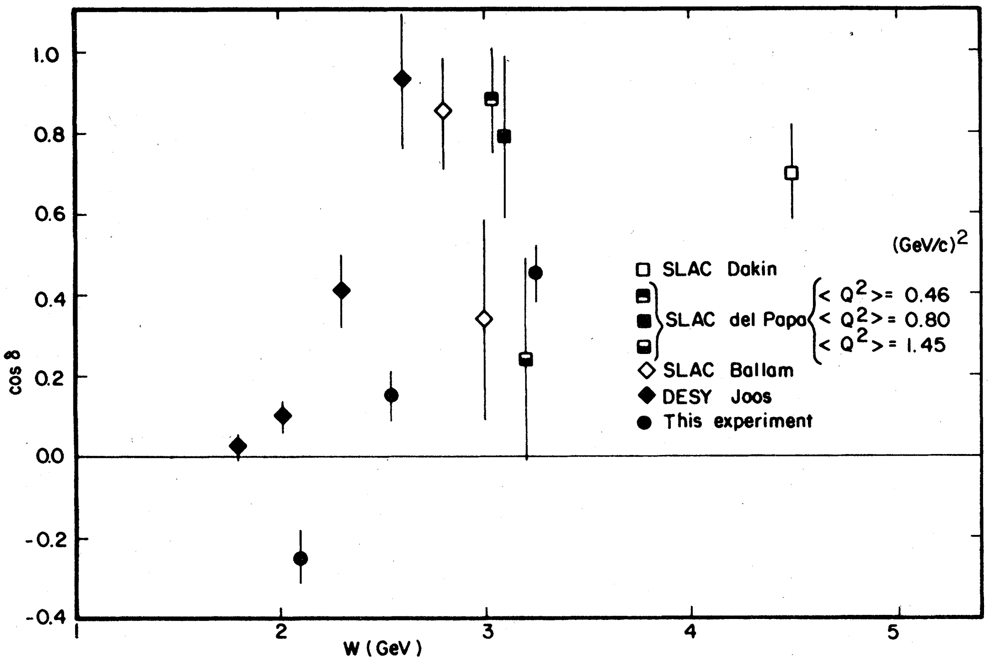

FIG. 20. cosδ, the phase difference between the longitudinal and transverse amplitudes plotted versus $W$. The data from this experiment are averaged over $Q^2$. Data from the experiments SLAC Dakin,[41] SLAC del Papa,[44] SLAC Ballam,[42] and DESY Joos[26] are included.

old in water ($p = 1.06$ GeV) but nevertheless gave a large pulse in one of the water counters. (f) We relied on the peaking approximation[22] in order to reduce the number of events in which the incident or scattered electron radiated a hard photon. We eliminated events in which the missing momentum was within 2.5° of the incident or scattered electron direction. (g) Finally, we rejected events in which the $\chi^2$ for the fit of all tracks to a common vertex was too large.

These cuts substantially reduced the background under the $\omega$ peak; Fig. 28 shows the final $m_{3\pi}$ distribution.

The data in the mass range of $0.6 < m_{3\pi} < 1$ GeV were fit to a Gaussian plus a background quadratic[55] in $m_{3\pi}$. The Gaussian and the background

TABLE VII. The $\rho^0$ electroproduction cross section $\sigma_\rho(Q^2,W)$ and the ratio $\sigma_\rho(Q^2,W)/\sigma_{\text{dif}}(Q^2,W)$ as functions of $W$ and $Q^2$.

| $W$ (GeV) | $Q^2$ (GeV$^2$) | $\sigma_\rho$ ($\mu$b) | $\sigma_\rho/\sigma_{\text{dif}}$ |
|---|---|---|---|
| 1.9–2.3 | 0.7–1.0 | 5.40±0.61 | 0.97±0.19 |
| | 1.0–1.3 | 2.26±0.25 | 0.70±0.13 |
| | 1.3–2.0 | 1.36±0.14 | 0.74±0.14 |
| | 2.0–4.0 | 0.57±0.09 | 0.86±0.29 |
| 2.3–2.9 | 0.7–1.0 | 2.76±0.20 | 0.83±0.10 |
| | 1.0–1.3 | 1.31±0.11 | 0.45±0.07 |
| | 1.3–2.0 | 0.78±0.06 | 0.55±0.07 |
| | 2.0–4.0 | 0.21±0.03 | 0.55±0.13 |
| 2.9–4.1 | 0.7–1.0 | 1.06±0.07 | 0.36±0.04 |
| | 1.0–1.3 | 0.62±0.05 | 0.23±0.04 |
| | 1.3–2.0 | 0.34±0.03 | 0.20±0.03 |
| | 2.0–4.0 | 0.19±0.02 | 0.27±0.06 |

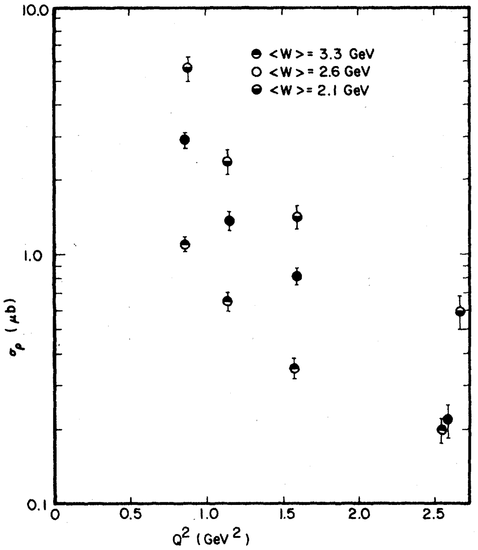

FIG. 21. The $\rho^0$ electroproduction cross section $\sigma_\rho(Q^2,W)$ measured in this experiment, plotted versus $Q^2$.

were both integrated over the 25-MeV mass bins used for the least-squares fit. The fit yielded a mass of 785±5 MeV and a standard deviation of 35±7 MeV for the Gaussian. Since our mass was consistent with the Particle Data Group[32] average of $m_\omega=783$ MeV, we used this value in the rest of the analysis. Our $\omega$ peak is considerably wider than the natural width, owing to measurement errors, so we have used our fit value of the width. The fit yielded a total of 670±57 events in the total data sample.

### C. The $\omega/\rho^0$ ratio

The ratio $\sigma_\omega(Q^2,W)/\sigma_\rho(Q^2,W)$ is independent of the largest corrections necessary to determine the individual cross sections. We have measured this ratio with the data grouped into two bins in $W$ with three bins in $Q^2$ and also for three bins in $W$ with two bins in $Q^2$. In order to reduce possible systematic effects due to changes in beam intensity or chamber efficiency, we selected a data sample taken in a continuous run representing about 72% of the integrated luminosity of the $\omega$ experiment.

In each $Q^2$-$W$ bin we obtained the $\omega$ yield by fitting the $m_{3\pi}$ distribution as described in the previous section. This yield was corrected for the branching ratio[32] $B(\omega\to\pi^+ +\pi^- +\pi^0)=(89.5\pm0.5)\%$. The $\omega$ yield was also corrected for losses due to cuts (a) through (e) in Sec. VIII B. We used the Monte Carlo simulation of the detec-

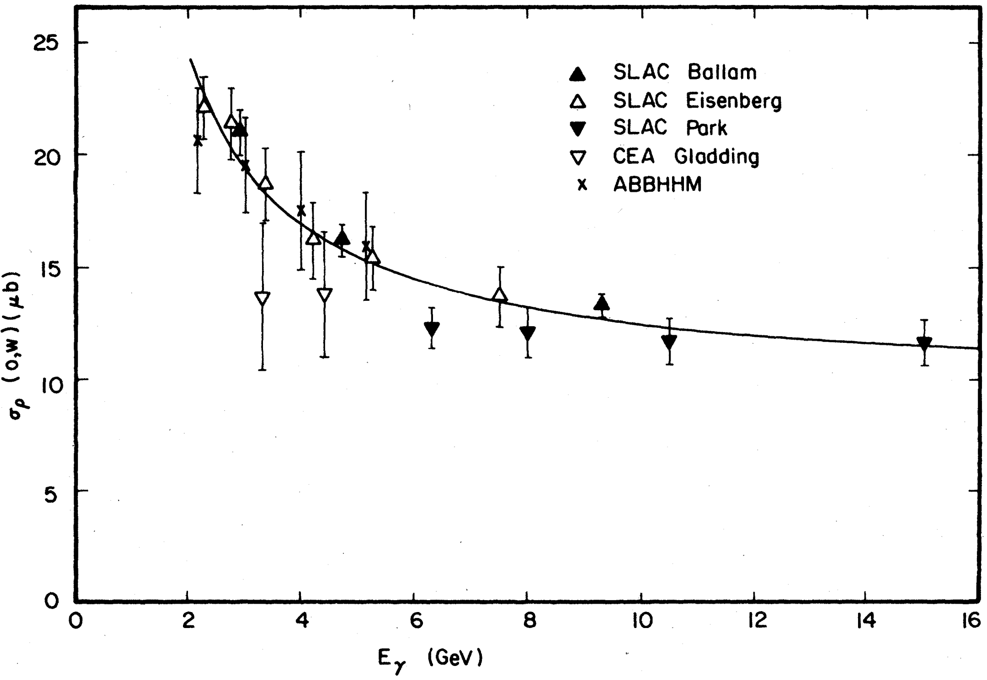

FIG. 22. The $\rho^0$ photoproduction cross section plotted against the photon energy $E_\gamma$. The curve is the fit described in the text. We have included data from the photoproduction experments, SLAC Ballam,[38] SLAC Eisenberg,[37] SLAC Park,[39] CEA Gladding,[40] and ABBHHM.[36]

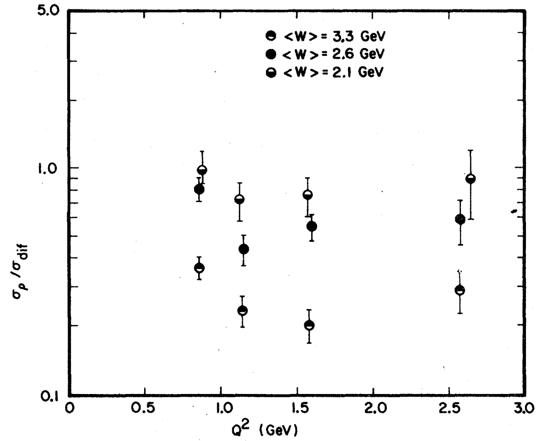

FIG. 23. The ratio $\sigma_p(Q^2,W)/\sigma_{\rm dif}(Q^2,W)$ for $\rho^0$ electroproduction for this experiment.

tor described in Sec. V to estimate these corrections. In the Monte Carlo calculation, we fixed the $m_{3\pi}$ mass at 783 MeV, we used an exponential $t$ distribution with $b_\omega = 5$ GeV$^{-2}$, and we used uniform distributions for $\Phi$, $\cos\theta$, and $\phi$ instead of the angular distribution in Eq. (18). We found that 20% of the $\omega$ events were lost to the neutron hypothesis and the 4C hypothesis, while an additional 20% were lost to the incorrect proton identification. The loss due to the radiative correction cut (f) was less than 2% and was neglected. Cut (g) on the $\chi^2$ for the vertex reconstruction rejected about 10% of the events, but no correction to the $\omega/\rho^0$ ratio was made for this cut since it should be the same for $\omega$ and $\rho^0$ yields. However, this correction was made in calculating absolute cross sections.

The $\rho^0$ yields were determined by fitting[1,2] the $m_{2\pi}$ distributions for the same data sample to a $\rho^0$ mass peak plus backgrounds due to the $\Delta^{++}$ and phase-space channels. (The $\Delta^0$ channel was neglected.) The $\rho^0$ and $\Delta^{++}$ distributions presented in Sec. VI were used in these fits, but a least-squares fit was used instead of the ML fit described there.

We obtained the $\omega/\rho^0$ ratios presented in Table VIII by dividing the corrected $\omega$ yields by the corresponding $\rho^0$ yields. The ratio $\sigma_\omega(Q^2,W)/\sigma_\rho(Q^2,W)$ as a function of $Q^2$ is illustrated in Fig. 29 along with data from other experiments. Our results show that the $\omega/\rho^0$ ratio at fixed $W$ is constant in the $Q^2$ interval $0 < Q^2 < 2$ GeV$^2$ for $2.2 < W < 3.7$ GeV. This agrees with the trend seen at lower $Q^2$ and $W$ in the SLAC del Papa,[44] DESY Joos,[53] and SLAC Ballam[42] experiments. We conclude that the $Q^2$ dependence of the OPE contribution is consistent with that of $\rho^0$ electroproduction, which is dominated by the square of the $\rho^0$ propagator in our measurements.

### D. The $\omega$ cross section $\sigma_\omega(Q^2,W)$

We extracted the cross section for $\omega$ electroproduction using a more conventional approach[4] than that used in the $\rho^0$ experiment. For each $Q^2$-$W$ bin, a weighted $\omega$ yield was obtained by first weighting each event with the inverse of the virtual-photon flux factor $\Gamma_W(Q^2,W)$ [Eq. (7)] calculated using the $Q^2$ and $W$ measured for the event, and then fitting the weighted $m_{3\pi}$ distribution to a Gaussian plus a smooth background as described in Sec. VIII B. The cross section $\sigma_\omega(Q^2,W)$ averaged over the $Q^2$-$W$ bin was then obtained by dividing this weighted yield by the number of incident electrons, the number of target protons/cm$^2$, the $Q^2$-$W$ widths of the bin, and the acceptance times efficiency properly averaged over the bin.[4] We present the results in Table IX, and we compare our measurements with other experiments in Fig. 30. The solid curves are $\sigma_\omega(0,W)/(1+Q^2/m_\omega{}^2)^2$. We see that our data appear to fall on these curves while the results of the DESY Joos[53] experiment tend to decrease less rapidly with $Q^2$. This behavior is actually too simple for the diffractive VMD prediction of Eq. (41), which decreases more rapidly with $Q^2$ than the square of the $\omega$ propagator, because both the photon flux factor $p_\gamma^*(0)/p_\gamma^*(Q^2)$ and the $t_{\rm min}$ correction decrease with $Q^2$. In Fig. 30 the dashed curves are the function

$$\sigma_b(Q^2,W) = \sigma_\omega(0,W)e^{-b_\omega|t_{\rm min}(Q^2)-t_{\rm min}(0)|} \qquad (43)$$

with $b_\omega = 6.1$ GeV$^{-2}$ (see Sec. VIII E). Clearly the high-$Q^2$ cross section must have a large contribution from something other than the diffractive VMD diagram.

### E. The $\omega$ forward peak

Since the OPE contribution is significant in our $Q^2$-$W$ region, we could not expect that the width of the forward $\omega$ peak is directly related to the simple diffraction picture that appears to dominate the forward $\rho^0$ peak. Furthermore, since the $\omega$ cross section is small, we could not measure the width of this peak for individual $Q^2$ and $W$ bins. We have extracted the cross section, $d\sigma_\omega/dt'$ in the $t'$ range $0 < t' < 1$ GeV$^2$, from our data with

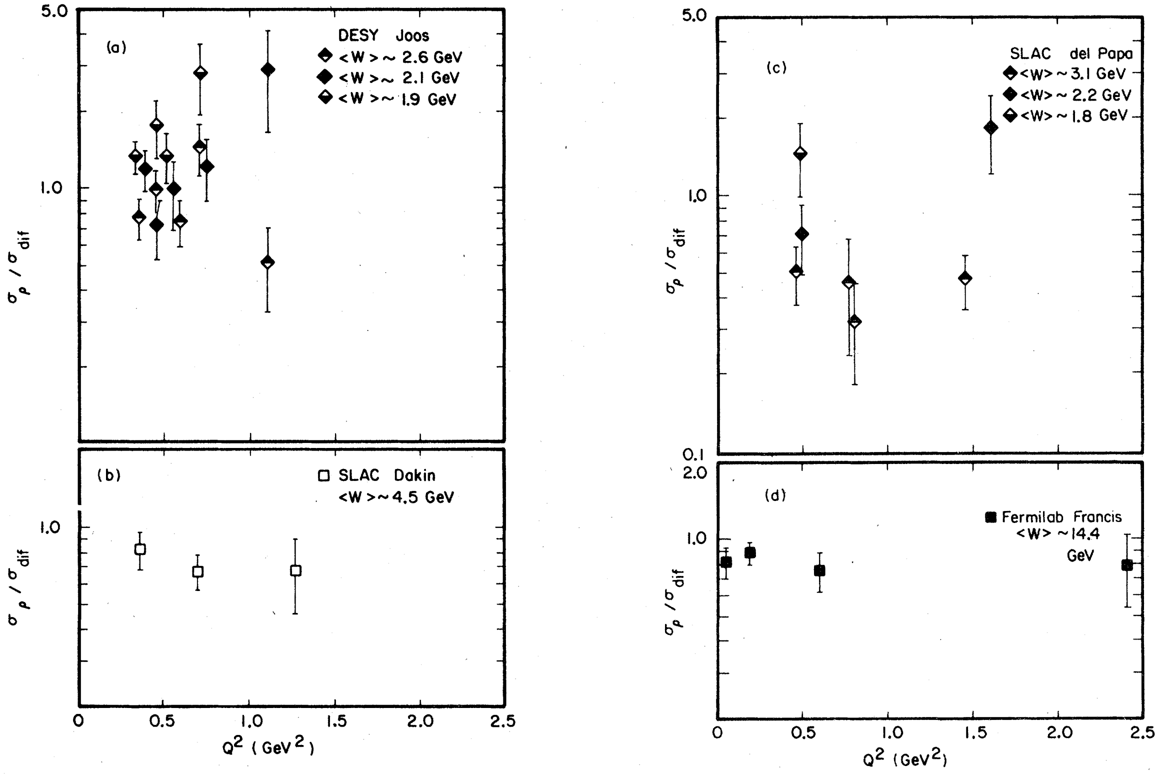

FIG. 24. The ratio $\sigma_\rho(Q^2,W)/\sigma_{\mathrm{dif}}(Q^2,W)$ for the $\rho^0$ electroproduction experiments, Fermilab Francis,[43] SLAC Dakin,[41] SLAC del Papa,[44] and DESY Joos,[26] versus $Q^2$. Data points with large errors have been arbitrarily excluded.

$0.5<Q^2<3$ GeV$^2$ and $2.25<W<3.7$ GeV. This cross section is plotted in Fig. 31. The data are consistent with an exponential $d\sigma_\omega/dt'=Ae^{-b_\omega t'}$ with $b_\omega=6.1\pm0.8$ GeV$^{-2}$. This is to be compared with $b_\omega=8.4\pm1.2$ GeV$^{-2}$ in photoproduction in this $W$ region.[38,36]

## IX. $\phi$ ANALYSIS AND RESULTS

### A. Expectations for $\phi$ electroproduction

Since the $\phi$ meson is composed of strange quarks, the diffraction diagram [Fig. 1(c)] should be the only important contribution[6,56,57] to $\phi$ electoproduction. The $\phi$ electroproduction cross section would then be given by Eq. (39),

$$\sigma_{\phi\,\mathrm{dif}}(Q^2,W)=\frac{\sigma_\phi(Q,W)}{(1+Q^2/m_\phi{}^2)^2}\,\frac{p_\gamma^*(0)}{p_\gamma^*(Q^2)}\times(1+\epsilon R_\phi)e^{-b_\phi|t_{\min}(Q^2)-t_{\min}(0)|}\,. \tag{44}$$

There is only one experiment[58] with significant $\phi$ electroproduction results. It measures $\phi$ electroproduction at $Q^2=0.23$, 0.43, and 0.97 GeV$^2$ with $W$ near 2.9 GeV. The authors conclude that $d\sigma_\phi/dt$ measured at $t=-0.6$ GeV$^2$ decreases as the square of the $\phi$ propagator. Our data extend the $Q^2$-$W$ range in which the diffractive VMD model is tested.

### B. Analysis of $e+p\rightarrow e+K^++K^-+p$ events

The kinematic fitting described in Sec. IV yielded a total of 839 $e+p\rightarrow e+K^++K^-+p$ events. Figure 32 illustrates the $K^+K^-$ effective mass $(m_{KK})$ distribution for a sample of these events. The $\phi$ meson peak is clearly visible just above the $K^+K^-$ threshold. We fit this mass distribution to a Gaussian and a phase-space background. The mass obtained from the fit was 1.021 GeV, in excellent agreement with the Particle Data Group average of 1.020 GeV. The standard deviation of the Gaussian was 0.011 GeV, due to the experimental resolution. Fig. 33 shows the $K^-p$

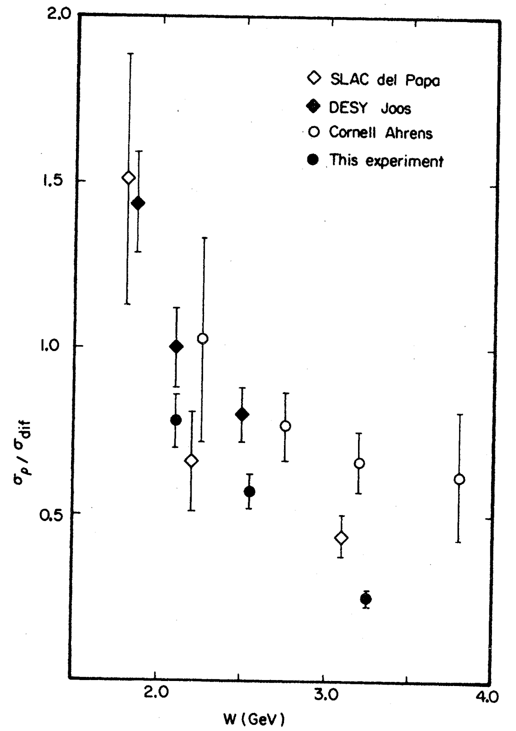

FIG. 25. The ratio $\sigma_\rho(Q^2,W)/\sigma_{\text{dif}}(Q^2,W)$ averaged over $Q^2$ and plotted versus $W$. Data from the SLAC del Papa,[44] DESY Joos,[28] and Cornell Ahrens[45] experiments are compared to the results of this experiment.

invariant-mass ($m_{Kp}$) distribution. The peak corresponds to the production of the $\Lambda^*(1520)$ and its subsequent decay in the $K^-p$ mode. We have previously reported our measurements of this channel.[20] Here we note that it is one of the reactions that could contribute to the background in the $m_{KK}$ distribution. In order to avoid contamination of the $\phi$ data by any possible kinematic reflection of the $\Lambda^*(1520)$ we have used data with $m_{Kp} > 1.6$ GeV in the $\phi$ analysis.

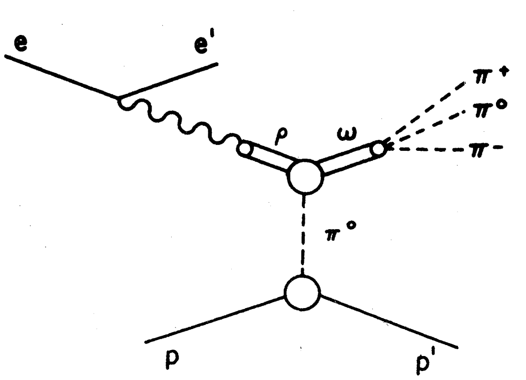

FIG. 26. The one-pion-exchange diagram for $\omega$ electroproduction.

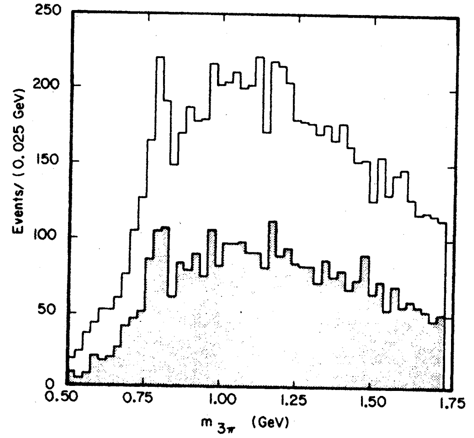

FIG. 27. The $m_{3\pi}$ distribution for events for which one of the two $p\pi^+\pi^-\pi^0$ hypotheses had the smallest value of the sum of the 1C $\chi^2$ and TOF $\chi^2$. There are 7230 events with no $t$ cut and in the shaded distribution there are 3290 events with $|t| < 0.5$ GeV$^2$.

We divided the data into two bins in $Q^2$ for all $W$ and two bins in $W$ for all $Q^2$. In each bin we calculated the $\phi$ weighted yield by weighting each event in the $m_{KK}$ distribution with $1/\Gamma_W(Q^2,W)$ and then fitting the distribution to a Gaussian plus phase space averaged over the appropriate $W$ range. We then obtained the $\phi$ cross section by dividing the weighted yield by the average of acceptance times efficiency, the number of incident electrons, the number of protons/cm$^2$ in the target, the widths of the $Q^2$ and $W$ bins, and the branching ratio[32] $B(\phi \to K^+ + K^-) = 0.486 \pm 0.012$. In the

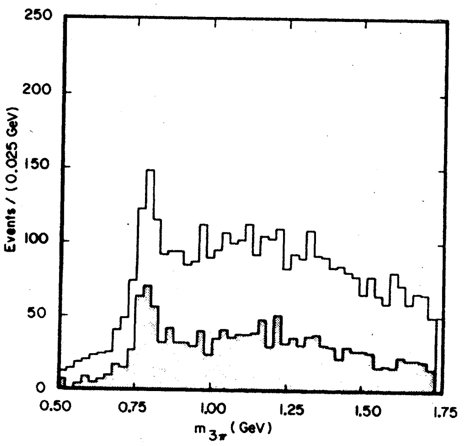

FIG. 28. The $m_{3\pi}$ distribution for events that pass cuts (a) through (g) in the text. There are 3776 events with no $t$ cuts, and in the shaded distribution there are 1394 events with $|t| < 0.5$ GeV$^2$.

TABLE VIII. The ratio $\sigma_\omega(Q^2,W)/\sigma_\rho(Q^2,W)$ for three bins in $Q^2$ and two bins in $W$ and for three bins in $W$ and two bins in $Q^2$.

| $W$ (GeV) | $\langle W \rangle$ (GeV) | $Q^2$ (GeV$^2$) | $\langle Q^2 \rangle$ (GeV$^2$) | $\sigma_\omega/\sigma_\rho$ |
|---|---|---|---|---|
| 2.2−2.7 | 2.5 | 0.7−1.1 | 0.9 | 0.31±0.09 |
| | | 1.1−1.4 | 1.2 | 0.25±0.16 |
| | | 1.4−3.0 | 1.9 | 0.62±0.22 |
| 2.7−3.7 | 3.2 | 0.7−1.1 | 0.9 | 0.12±0.06 |
| | | 1.1−1.4 | 1.2 | 0.32±0.16 |
| | | 1.4−3.0 | 1.9 | 0.16±0.08 |
| 2.2−2.6 | 2.4 | 0.7−1.2 | 1.0 | 0.31±0.09 |
| | | 1.2−3.0 | 1.8 | 0.39±0.17 |
| 2.6−3.2 | 2.9 | 0.7−1.2 | 1.0 | 0.20±0.06 |
| | | 1.2−3.0 | 1.8 | 0.41±0.09 |
| 3.2−3.7 | 3.5 | 0.7−1.2 | 1.0 | 0.05±0.08 |
| | | 1.2−3.0 | 1.8 | 0.08±0.08 |

Monte Carlo acceptance-efficiency calculation we used a fixed mass for the $\phi$, an exponential $t$ distribution with $b_\phi=4$ GeV$^{-2}$, and uniform distributions in the angles $\Phi$, $\cos\theta$, and $\phi$, instead of the angular distribution in Eq. (18).

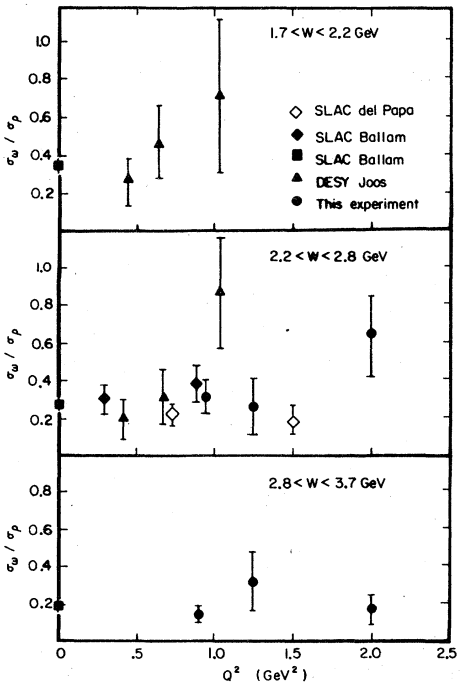

FIG. 29. The $\omega/\rho^0$ ratio $\sigma_\omega(Q^2,W)/\sigma_\rho(Q^2,W)$ vs $Q^2$ from this experiment compared with the SLAC del Papa,[44] DESY Joos,[53] and SLAC Ballam[42] electroproduction experiments, and the SLAC Ballam[38] photoproduction experiment.

### C. The $\phi$ forward peak

In order to compare cross sections to the diffractive production model, we require the slope parameter $b_\phi$ of the forward $\phi$ peak. In order to estimate $b_\phi$ from our data, we divided all of our data into two bins in $t'=|t-t_{\min}|$ ($0<t'<0.2$ GeV$^2$ and $0.2<t'<0.6$ GeV$^2$). We then calculated the $\phi$ cross section for these $t'$ bins, as described above, and obtained the slope value $b_\phi=3.2\pm1.2$ GeV$^{-2}$ from the two data points. Figure 34 compares our result with those of other photoproduction[59−61] and electroproduction[58] experiments. Although visible, the decrease of $b_\phi$ with $c\Delta\tau$ is less pronounced than it was in $\rho^0$ electroproduction (Fig. 14). Since our measurement of $b_\phi$ is consistent with the Cornell Dixon[58] results at lower $Q^2$, we have adopted their average value $b_\phi=3.46\pm0.22$ GeV$^{-2}$ for comparing our cross sections with the diffractive VMD model.

### D. The $\phi$ cross section $\sigma_\phi(Q^2,W)$

The $\phi$ cross sections obtained from the analysis described in Sec. VIII B are presented in Table X. In order to compare these cross sections with the diffractive VMD model, we need $\sigma_\phi(0,W)$ and $R_\phi$. Since we do not measure $R_\phi$, we extrapolate the result, $R_\phi=\xi^2Q^2/m_\phi{}^2$, with $\xi^2=0.33\pm0.08$, of the Cornell Dixon[58] experiment. Our maximum value of $Q^2$ is 2.4 GeV$^2$, so this extrapolation is reasonable even if $R_\phi$, like $R_\rho$, becomes constant between 0.5 and 1 at large $Q^2$. Figure 35 shows $\sigma_\phi(0,W)$; above $W=2.4$ GeV, it is constant with an average

TABLE IX. The $\omega$ electroproduction cross section $\sigma_\omega(Q^2,\omega)$.

| $W$ (GeV) | $\langle W\rangle$ (GeV) | $Q^2$ (GeV$^2$) | $\langle Q^2\rangle$ (GeV$^2$) | $\sigma_\omega$ ($\mu$b) |
|---|---|---|---|---|
| 1.7–2.3 | 2.0 | 0.7–1.3 | 1.0 | $1.15\pm0.18$ |
| | | 1.3–3.0 | 2.0 | $0.68\pm0.15$ |
| 2.3–3.7 | 2.8 | 0.7–1.3 | 1.0 | $0.45\pm0.08$ |
| | | 1.3–3.0 | 2.0 | $0.23\pm0.05$ |

value of $\sigma_\phi(0,W)=0.45\pm0.02$ $\mu$b. The lower value of $\sigma_\phi(0,W)$ for the Bonn Besch[60] experiment at $W=2.1$ GeV is largely due to $t_{\min}$.

Figure 36 illustrates the ratio $\sigma_\phi(Q^2,W)/\sigma_{\text{dif}}(Q^2,W)$ for this experiment and the Cornell Dixon[58] experiment. Our results for this ratio are constant as a function of $Q^2$ and extrapolate to the low-$Q^2$ Cornell Dixon results. However, this ratio increases as $Q^2$ increases in the Cornell Dixon experiment. We also note that the $W$ dependence of $\sigma_\phi(Q^2,W)$ in Table X is consistent with the $W$ dependence of the $\rho^0$ cross-section ratio.

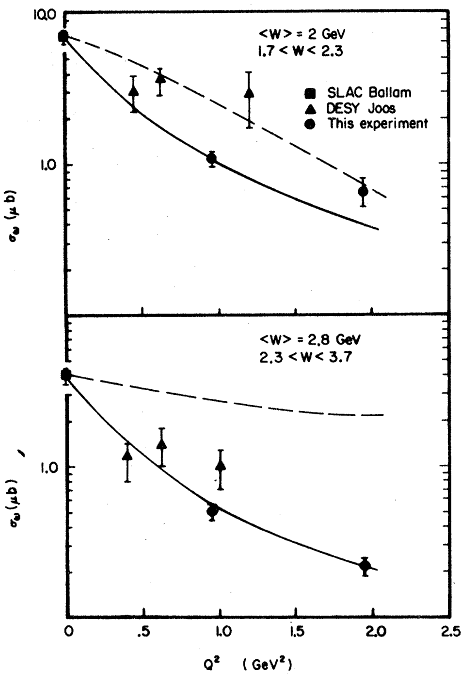

FIG. 30. The $\omega$ cross section $\sigma_\omega(Q^2,W)$ vs $Q^2$ for two $W$ intervals. The SLAC Ballam[38] photoproduction data and the DESY Joos[53] electroproduction data are included for comparison. The solid curves are $\sigma_\omega(0,W)/(1+Q^2/m_\omega{}^2)^2$, and the dashed curves are $\sigma_\omega(0,W)$ corrected for $t_{\min}$ according to Eq. (43).

## X. CONCLUSIONS

With our large sample of 4C $\rho^0$ events in the $Q^2$-$W$ range $0.7<Q^2<4$ GeV$^2$ and $1.9<W<4$ GeV we find the following.

(a) The forward diffraction peak for $\rho^0$ electroproduction becomes very broad as the formation time $c\Delta\tau$ decreases below 1 fm.

(b) The diffraction peak for longitudinal $\rho^0$'s is broader than that for transverse $\rho^0$'s.

(c) The longitudinal-transverse cross-section ratio $R_\rho$ is constant above $Q^2=1$ GeV$^2$ in contrast to its linear rise with $Q^2$ at lower $Q^2$.

(d) The diffractive VMD model comes close to describing the $Q^2$ dependence of the $\rho^0$ total cross section. However, the model utterly fails to reproduce the rapid decrease in the cross section with

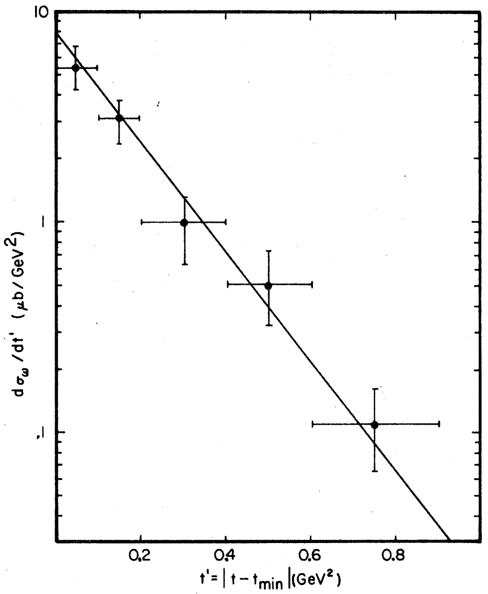

FIG. 31. The cross section $d\sigma_\omega/dt'$ vs $t'$. The straight line is the fit to the form $d\sigma_\omega/dt'=Ae^{-b_\omega t'}$ with $b_\omega=6.1$ GeV$^2$.

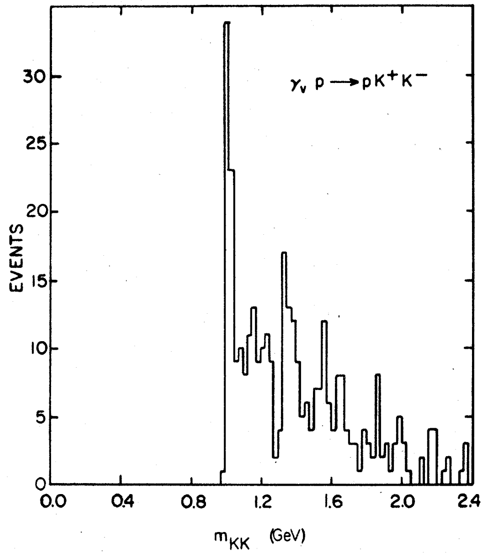

FIG. 32. The $m_{KK}$ distribution.

increasing $W$ that we observe. We note that the trend of earlier experiments agrees with our more precise results.

With a smaller sample of 1C $\omega$ events in the $Q^2$-$W$ range $0.7 < Q^2 < 3$ GeV$^2$ and $2.25 < W < 3.7$ GeV we observe the following.

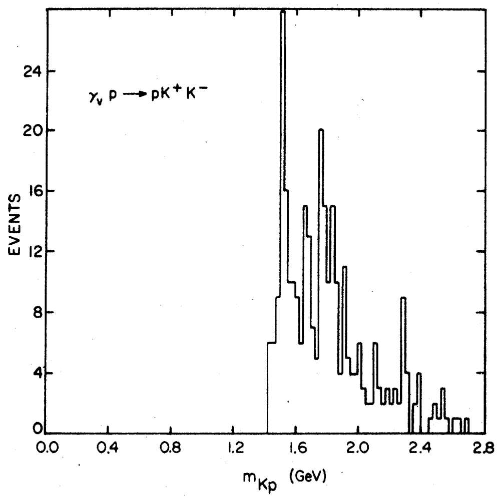

FIG. 33. The $m_{Kp}$ distribution.

(e) The $\omega/\rho^0$ ratio is independent of $Q^2$ at fixed $W$. Our $\omega/\rho^0$ results are also consistent with photoproduction data at the same $W$.

(f) We find that the diffractive VMD model grossly underestimates the $\omega$ cross section at high $Q^2$.

We were able to measure $\phi$ electroproduction in the range $0.8 < Q^2 < 4$ GeV$^2$ and $2 < W < 3.7$ GeV.

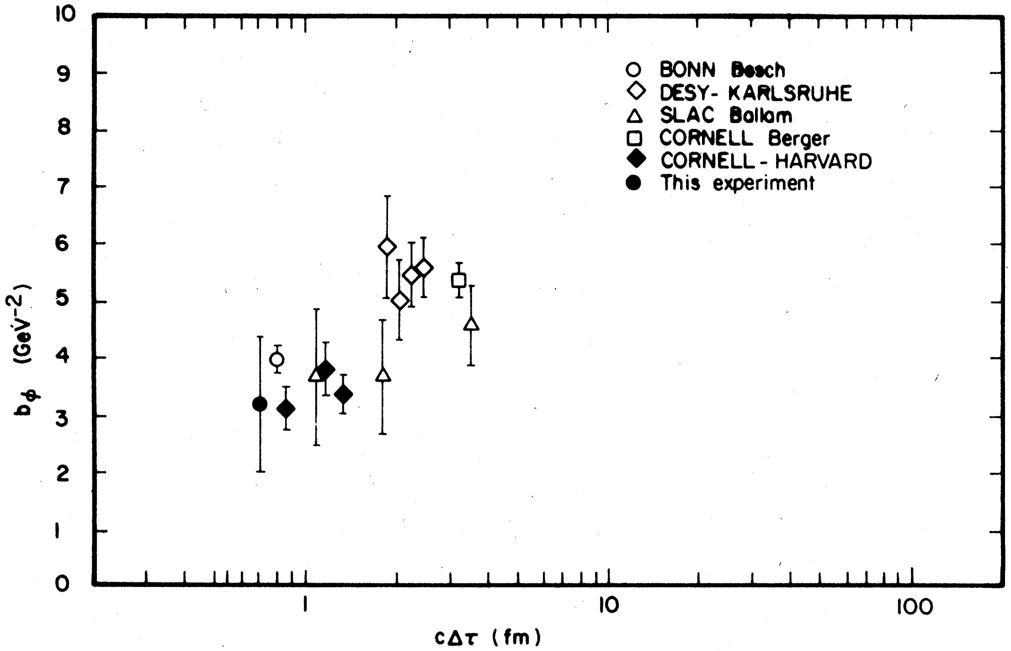

FIG. 34. The $\phi$ slope parameter $b_\phi$ versus the formation time $c\Delta\tau$ for this experiment compared to the results of the Cornell Dixon[58] electroproduction experiment and to the SLAC Ballam,[38] Cornell Berger,[59] Bonn Besch,[60] photoproduction experiments.

TABLE X. The $\phi$ electroproduction cross section $\sigma_\phi(Q^2,W)$ and the ratio $\sigma_\phi(Q^2,W)/\sigma_{\phi\,\mathrm{dif}}(Q^2,W)$ for two values of $Q^2$ in one $W$ interval and for two values of $W$ in one interval of $Q^2$.

| $W$ (GeV) | $\langle W\rangle$ (GeV) | $Q^2$ (GeV$^2$) | $\langle Q^2\rangle$ (GeV$^2$) | $\sigma_\phi$ (nb) | $\sigma_\phi/\sigma_{\mathrm{dif}}$ |
|---|---|---|---|---|---|
| 2.0–3.7 | 2.8 | 0.8–1.25 | 1.1 | 59±15 | 0.61±0.17 |
| | 2.7 | 1.25–4.0 | 2.4 | 17±5 | 0.67±0.21 |
| 2.0–3.0 | 2.5 | 0.8–4.0 | 2.2 | 25±8 | 1.09±0.37 |
| 3.0–3.7 | 3.3 | | 2.1 | 14±5 | 0.30±0.11 |

Our results show the following.

(g) The diffractive VMD model agrees with the $Q^2$ dependence of our data, but it predicts a larger cross section than we observe.

Although $\rho^0$, $\omega$, and $\phi$ electroproduction exhibit some of the features of the diffractive VMD model, the $W$ dependence we observe demands a more complete theoretical understanding.

## ACKNOWLEDGMENTS

This paper is a final report of an extended study which involved the contributions of many individuals besides the authors. We thank Professor Boyce D. McDaniel for his support of this experiment and Professor Maury Tigner for his assistance as director of synchrotron operations during the course of this experiment. This experiment required extremely stable operation of the synchrotron and the extracted beam. The excellent performance of the machine in the closing stages of its life as a fixed-target facility were a credit to the operating crew led by Dr. Gerry Rouse and to the people who designed and built the machine. Apart from the staff of the Wilson Laboratory, many undergraduates contributed to the experiment. Although their financial rewards were modest, we

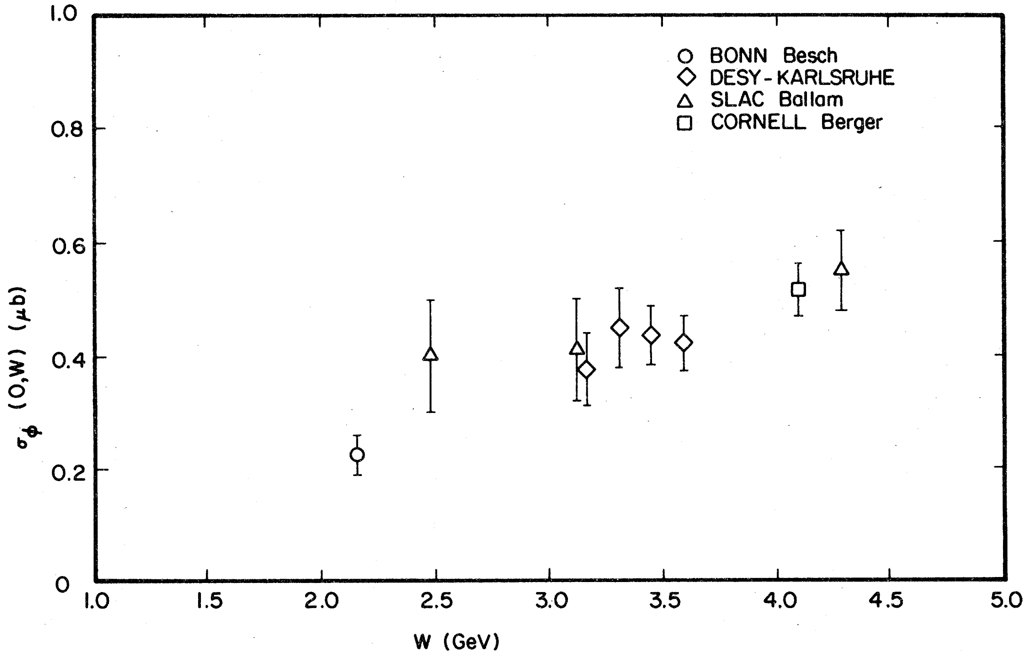

FIG. 35. The $\phi$ photoproduction cross sections $\sigma_\phi(0,W)$ used in comparing diffractive VMD to this experiment plotted versus $W$. Data from the SLAC Ballam,[38] Cornell Berger,[59] Bonn Besch,[60] and DESY Behrend[61] experiments are plotted.

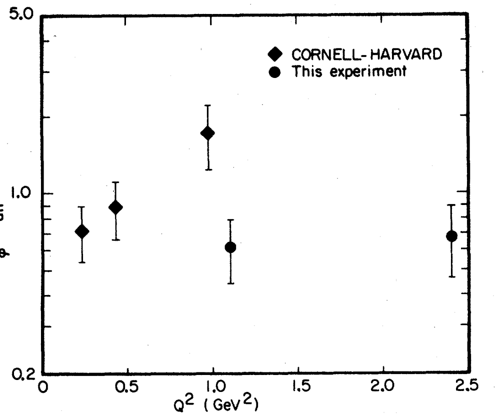

FIG. 36. The ratio $\sigma_\phi(Q^2,W)/\sigma_{\rm dif}(Q^2,W)$ vs $Q^2$ for this experiment and the Cornell Dixon[58] experiment.

hope that the learning experience was as valuable for them as it was for us. This work was supported in part by the National Science Foundation.

## APPENDIX A: DIFFERENTIAL YIELDS FOR THE MAXIMUM-LIKELIHOOD FITS

In order to use the method of maximum liklihood, it is necessary to write the differential yield as a sum of terms differential in a single common variable $\vec v$.

$$y(\vec v_\gamma,\vec v)=y_\rho(\vec v_\gamma,\vec v)+y_{++}(\vec v_\gamma,\vec v)+y_0(\vec v_\gamma,\vec v)+y_{\rm PS}(\vec v_\gamma,\vec v)\ . \tag{A1}$$

In this expression, $\vec v$ could be any five variables that describe the final $\pi^+\pi^-p$ state. However, it is desirable to have functions in the individual terms in Eq. (A1) that are differential in variables natural for each channel. The natural variables for the $\rho^0$, $\Delta^{++}$, $\Delta^0$, and PS channels are

$$\vec v_\rho=(m_{\pi\pi}{}^2,t',\Phi,\cos\theta,\phi)\ , \tag{A2a}$$

$$\vec v_{++}=(m_{++}{}^2,t'_{++},\Phi_{++},\cos\theta_+,\phi_+)\ , \tag{A2b}$$

$$\vec v_0=(m_0{}^2,t'_0,\Phi_0,\cos\theta_-,\phi_-)\ , \tag{A2c}$$

$$\vec v_{\rm PS}=(m_{\pi\pi}{}^2,m_{++}{}^2,\alpha,\cos\beta,\gamma)\ . \tag{A2d}$$

The angle $\Phi_{++}$ ($\Phi_0$) is the azimuthal angle of the $\Delta^{++}$ ($\Delta^0$) production plane, and the angles $\theta_+$ ($\theta_-$), $\phi_+$ ($\phi_-$) are the polar and azimuthal angles of the $\pi^+$ ($\pi^-$) from the decay of the $\Delta^{++}$ ($\Delta^0$). These angles are analogous to the $\rho^0$ production and decay angles[26] used earlier. Following convention, we chose $m_{\pi\pi}{}^2$ and $m_{++}{}^2$ for the phase-space variables. The angles $\alpha$, $\beta$, and $\gamma$ are Euler angles describing the orientation of the plane of the $\pi^+$, $\pi^-$, and $p$ vectors in the $\gamma_V p$ center of mass. For the common variables $\vec v$ we choose

$$\vec v=(E_+,E_-,\alpha',\cos\beta',\gamma')\ , \tag{A3}$$

where $E_+$ ($E_-$) is the $\pi^+$ ($\pi^-$) energy, and $\alpha'$, $\beta'$, and $\gamma'$ are again Euler angles describing the orientation of the $\pi^+\pi^-p$ plane. Using Jacobians, the total of a sum of four yields given by Eq. (28) can be expressed as a differential in the common variable $v$:

$$\begin{aligned}y(\vec v_\gamma,\vec v)=&y_\rho(\vec v_\gamma,\vec v_\rho)J(\vec v_\rho\,|\,\vec v)\\&+y_{++}(\vec v_\gamma,\vec v_{++})J(\vec v_{++}\,|\,\vec v)\\&+y_0(\vec v_\gamma,\vec v_0)J(\vec v_0\,|\,\vec v)\\&+y_{\rm PS}(\vec v_\gamma,\vec v_{\rm PS})J(\vec v_{\rm PS}\,|\,\vec v)\ .\end{aligned} \tag{A4}$$

Following Jackson[23] it can be shown that the Jacobians are

$$J(\vec v_\rho\,|\,\vec v)=4Wq\frac{m_{\pi\pi}}{q_{\pi\pi}}\ , \tag{A5a}$$

$$J(\vec v_{++}\,|\,\vec v)=4Wq\frac{m_{++}}{q_{++}}\ , \tag{A5b}$$

$$J(\vec v_0\,|\,\vec v)=4Wq\frac{m_0}{q_0}\ , \tag{A5c}$$

$$J(\vec v_{\rm PS}\,|\,\vec v)=4W^2\ . \tag{A5d}$$

Here $q$ is the virtual-photon momentum in the $\gamma_V p$ center of mass, and $q_{\pi\pi}$, $q_{++}$, and $q_0$ have been defined in Sec. IV. The $m_{\pi\pi}/q_{\pi\pi}$, $m_{++}/q_{++}$, and $m_0/q_0$ factors have been used in analyzing previous experiments,[26,38] but the factors $4Wq$ and $4W^2$ were not. In principle, these factors amount to an unnecessary normalization convention if all of the data included in a single fit are at a fixed $W$ or are in a small range of $W$. Since we fitted data over a rather wide range of $W$ and we were especially concerned with possible systematic errors in the $W$ dependence, we felt that it was more prudent to keep these factors.

To convert a differential yield written in the form of Eq. (28) to a term in Eq. (A1), it is necessary to replace $f_\rho(\vec v_\rho)$ with $g_\rho(\vec v)$ given by

$$g_\rho(\vec v)=4Wq\frac{m_{\pi\pi}}{q_{\pi\pi}}f_\rho(\vec v_\rho)\ . \tag{A6}$$

## APPENDIX B: REMARKS ON THE MAXIMUM-LIKELIHOOD FITS

A maximum-likelihood function can be constructed from the data using the normalized probability density defined in Eq. (31). If the events actually observed in the $Q^2$-$W$ bin being fitted are represented by the vector $\vec{V}$

$$\vec{V}=\{\vec{v}_{\gamma 1},\vec{v}_1,\vec{v}_{\gamma 2},\vec{v}_2,\ldots,\vec{v}_{\gamma N},\vec{v}_N\}\ , \tag{B1}$$

the likelihood function $L'(\vec{V}\mid\vec{a})$ would be

$$L'(\vec{V}\mid\vec{a})=\sum_{i=1}^{N} p(\vec{v}_{\gamma i},\vec{v}_i\mid\vec{a})\ . \tag{B2}$$

However, this likelihood function has too many parameters; the numerator and denominator of $p(\vec{v}_\gamma,\vec{v}\mid\vec{a})$ are both linear in the coefficients $A$, so these coefficients are determined by $L'(\vec{V}\mid\vec{a})$ only up to a multiplicative constant. Obviously the total yield

$$Y=A_\rho H_\rho+A_{++}H_{++}+A_0H_0+A_{\text{PS}}H_{\text{PS}} \tag{B3}$$

should be fixed to equal to the total number of events observed in the experiment. This can be accomplished by setting $Y=N$ and eliminating one of the coefficients $A_\rho$, $A_{++}$, $A_0$, or $A_{\text{PS}}$ from $p(\vec{v}_\gamma,\vec{v}\mid\vec{a})$ and hence from $L'(\vec{V}\mid\vec{a})$. We have chosen another method[62] which simplifies the calculations involved in maximizing the likelihood. If the total predicted yield is $Y$, the Poisson probability of observing $N$ events is $Y^Ne^{-Y}/N!$. Define a new likelihood function

$$L(\vec{V}\mid\vec{a})=L'(\vec{V}\mid\vec{a})\frac{Y^Ne^{-Y}}{N!}\ . \tag{B4}$$

The inclusion of the Poisson probability factor constrains $Y$ to be near to, but not necessarily equal to, $N$. Notice that the $Y^N$ factor in the Poisson probability will exactly cancel the $N$ factors of $Y$ from the denominator of $p(\vec{v}_\gamma,\vec{v}\mid\vec{a})$. The logarithm of the likelihood function then becomes

$$w(\vec{V}\mid\vec{a})=-\ln L(\vec{V}\mid\vec{a}) \tag{B5a}$$

$$=Y-\sum_{i=1}^{N}\ln g(\vec{v}_{\gamma i},\vec{v}_i\mid\vec{a})-\sum_{i=1}^{N}\ln[\Gamma_W(\vec{v}_{\gamma i})e(\vec{v}_{\gamma i},\vec{v}_i)]+\ln N! \tag{B5b}$$

$$=Y-\sum_{i=1}^{N}\ln g(\vec{v}_{\gamma i},\vec{v}_i\mid\vec{a})-w'(\vec{V})\ , \tag{B5c}$$

where the acceptance times efficiency function $e(\vec{v}_\gamma,\vec{v})$ appears explicitly only in the function $w'(\vec{V})$ which does not contain the parameters $\vec{a}$ to be fit. Hence $e(\vec{v}_\gamma,\vec{v})$ does not appear explicitly in any of the derivatives necessary to find the minimum of $w(\vec{V}\mid\vec{a})$ or the maximum of $L(\vec{V}\mid\vec{a})$. $e(\vec{v}_\gamma,\vec{v})$ does appear implicitly in $w(\vec{V}\mid\vec{a})$ through the integrals for $H_\rho$, $H_{++}$, $H_0$, and $H_{\text{PS}}$, but these integrals can be evaluated with a Monte Carlo integration. Therefore it is not necessary to calculate $e(\vec{v}_\gamma,\vec{v})$ as an explicit function.

## APPENDIX C: RELATIONSHIP BETWEEN YIELDS AND CROSS SECTIONS

In Eq. (23), we wrote the total $\rho^0$ yield in a given $Q^2W$ bin in the form

$$Y_\rho=N_en_H\int\Gamma_w(\vec{v}_\gamma)c_\rho s_\rho(\vec{v}_\gamma)f_\rho(\vec{v}_\rho)e(\vec{v}_\gamma,\vec{v}_\rho)d^3V_\gamma d^5V_\rho\ , \tag{C1}$$

and in Eq. (32) we defined this integral to be $H_\rho$,

$$H_\rho=\int s_\rho(\vec{v}_\gamma)f_\rho(\vec{v}_\rho)\Gamma_w(\vec{v}_\gamma)e(\vec{v}_\gamma,\vec{v})d^3V_\gamma d^5V_\rho\ , \tag{C2}$$

so, since $A_\rho=N_en_Hc_\rho$,

$$Y_\rho=N_en_Hc_\rho H_\rho=A_\rho H_\rho\ . \tag{C3}$$

According to Eq. (27), the cross section at fixed $Q^2$-$W$ is given by

$$\sigma_\rho(\vec{v}_\gamma)=c_\rho s_\rho(\vec{v}_\gamma)\int f_\rho(\vec{v}_\rho)d^5V_\rho\ , \tag{C4}$$

so the cross section averaged over a $Q^2$-$W$ bin is

$$\langle\sigma_\rho\rangle=\frac{c_\rho}{\Delta Q^2\Delta W2\pi}\int s_\rho(\vec{v}_\gamma)f_\rho(\vec{v}_\rho)d^5V_\rho d^3V_\gamma\ . \tag{C5}$$

In this expression, $\Delta Q^2$ and $\Delta W$ are the widths of the bin in $Q^2$ and $W$, respectively. With the definition

$$F_\rho=\int s_\rho(\vec{v}_\gamma)f_\rho(\vec{v}_\rho)d^5V_\rho d^3V_\gamma\ . \tag{C6}$$

Eq. (C5) becomes

$$\langle\sigma_\rho\rangle=\frac{c_\rho F_\rho}{\Delta Q^2\Delta W2\pi}\ . \tag{C7}$$

Combining this equation with Eq. (C3), the cross section averaged over a $Q^2$-$W$ bin is then

$$\langle\sigma_\rho\rangle=\frac{A_\rho}{N_en_H}\frac{F_\rho}{\Delta Q^2\Delta W2\pi}\ . \tag{C8}$$

[*] Present address: Brookhaven National Laboratory, Upton, New York 11973.

[†] Present address: Lawrence Berkeley Laboratory, Berkeley, California 94702.

[‡] Present address: Fermi National Accelerator Laboratory, P.O. Box 500, Batavia, Illinois 60510.

[§] Present address: Fairchild Republic, Farmingdale, New York 11735.

[||] Present address: Rockefeller University Group, CERN, 1211 Geneva 23, Switzerland.

[1] L. A. Ahrens *et al.*, Phys. Rev. Lett. 42, 208 (1979).

[2] L. A. Ahrens, Ph. D. thesis, Cornell University, 1978 (unpublished).

[3] J. T. Linnemann *et al.*, Phys. Rev. Lett. 41, 1266 (1978).

[4] J. T. Linnemann, Ph. D. thesis, Cornell University, 1978 (unpublished).

[5] C. T. Day, Ph. D. thesis, Cornell University, 1978 (unpublished).

[6] T. H. Bauer, R. D. Spital, D. R. Yennie, and F. M. Pipkin, Rev. Mod. Phys. 50, 261 (1978).

[7] H. T. Nieh, Phys. Lett. 38B, 100 (1972).

[8] There has been some discussion of how these two pictures could be limiting cases of the same description. See, for example, R. D. Spital and D. Y. Yennie, Nucl. Phys. 106, 269 (1976).

[9] L. A. Ahrens *et al.*, Nucl. Instrum. and Methods 173, 537 (1980).

[10] K. Berkelman, in *Proceedings of the 1971 International Symposium on Electron and Photon Interactions at High Energies,* edited by N. B. Mistry (Laboratory of Nuclear Studies, Cornell University, Ithaca, N.Y., 1972).

[11] L. N. Hand, Phys. Rev. 129, 1834 (1963).

[12] C. W. Akerlof *et al.*, Phys. Rev. 163, 1482 (1969).

[13] D. J. Harding, Ph. D. thesis, Cornell University, 1978 (unpublished).

[14] T. J. Killian, Ph. D. thesis, Cornell University, 1978 (unpublished).

[15] J. Klinger, Ph. D. thesis, Cornell University, 1978 (unpublished).

[16] E. A. Treadwell, Ph. D. thesis, Cornell University, 1978 (unpublished).

[17] H. Wind, Nucl. Instrum. and Methods 69, 122 (1969).

[18] We used the standard magic gas mixture suggested by G. Charpak *et al.*, Nucl. Instrum. and Methods 99, 279 (1972).

[19] Trademark of the Digital Equipment Corporation, Maynard, Massachusetts.

[20] C. T. Day *et al.*, Phys. Rev. D 23, 576 (1981).

[21] B. G. Gibbard *et al.*, Phys. Rev. Lett. 42, 1593 (1979).

[22] L. M. Mo and Y. S. Tsai, Rev. Mod. Phys. 41, 205 (1969).

[23] J. D. Jackson, Nuovo Cimento 34, 1644 (1964).

[24] M. Ross and L. Stodolsky, Phys. Rev. Lett. 17, 563 (1966); Phys. Rev. 149, 1172 (1966).

[25] P. Söding, Phys. Lett. 19, 702 (1966).

[26] P. Joos *et al.*, Nucl. Phys. B113, 53 (1976).

[27] We use the definitions of the angles $\Phi$, $\theta$, and $\phi$ given in Appendix A of the preceding reference. In evaluating these angles, it is important to avoid the temptation to move from the laboratory frame to the $\gamma_V p$ center of mass and thence to the $\rho^0$ rest frame by a succession of Lorentz boosts. Noncollinear Lorentz boosts do not form a group as was realized long ago in understanding Thomas precession.

[28] K. Schilling and G. Wolf, Nucl. Phys. B61, 381 (1973).

[29] H. L. Anderson, in *Proceedings of the 6th Annual Rochester Conference on High-Energy Nuclear Physics, 1956,* edited by J. Ballam *et al.* (Interscience, New York, 1956) pp. 20–22.

[30] This fact is discussed in most books on statistics. See, for example, S. Brandt, *Statistical and Computational Methods in Data Analysis* (North-Holland, Amsterdam, 1970).

[31] Actually, in order to include resolution in the expression for the yield, $e(\vec{v}_\gamma, \vec{v}_\rho)$ should be the kernel in an integral transform. Resolution effects are negligible in this experiment. For example, using the Monte Carlo calculation, we found that the rms resolution in $m_{\pi\pi}$ is approximately 11 MeV, which is negligible compared to $\Gamma_\rho$. Other resolution effects are even smaller.

[32] Particle Data Group, Rev. Mod. Phys. 52, S1 (1980).

[33] G. Kramer and H. R. Quinn, Nucl. Phys. B55, 222 (1973).

[34] Since the $\Delta^0$ contribution is small, $b_0$ was poorly determined by the fit. We fixed $b_0$ to 8 GeV$^{-2}$ in the fits to avoid runaway solutions.

[35] Actually not all parameters in Eq. (33) could be determined from a fit to data in such a narrow $t'$ range. We fixed $b_\rho = 3.5$ GeV$^{-2}$, $b_{++} = b_0 = 8$ GeV$^{-2}$, and $A_{\mathrm{PS}} = 0$. The results are not sensitive to the values of these parameters.

[36] Aachen-Berlin-Bonn-Hamburg-Heidelberg-München Collaboration, Phys. Rev. 175, 1669 (1968).

[37] Y. Eisenberg *et al.*, Phys. Rev. D 5, 15 (1972).

[38] J. Ballam *et al.*, Phys. Rev. D 5, 545 (1972); 7, 3150 (1973).

[39] J. Park *et al.*, Nucl. Phys. B36, 404 (1972).

[40] G. Gladding *et al.*, Phys. Rev. D 8, 3721 (1973).

[41] J. T. Dakin *et al.*, Phys. Rev. D 8, 687 (1973).

[42] J. Ballam *et al.*, Phys. Rev. D 10, 765 (1974).

[43] W. Francis *et al.*, Phys. Rev. Lett. 38, 633 (1977).

[44] C. del Papa *et al.*, Phys. Rev. D 19, 1303 (1979).

[45] L. Ahrens *et al.*, Phys. Rev. D 9, 1894 (1974).

[46] H. Cheng and T. T. Wu, Phys. Rev. 183, 1324 (1969).

[47] J. D. Bjorken *et al.*, Phys. Rev. D 3, 1382 (1971); J. D. Bjorken, in *Proceedings of the 1971 International Symposium on Electron and Photon Interactions at High Energies* (Ref. 10).

[48] For example, if we were to first integrate $W(\cos\theta, \psi)$ over $\psi$ and then do the ML fits, we would obtain $R_\rho$ values that would be systematically low by approximately 15%.

[49] H. Fraas and D. Schildknecht, Nucl. Phys. B14, 543

(1969).

[50] G. Wolf, in *Proceedings of the 1971 International Symposium on Electron and Photon Interactions at High Energies* (Ref. 10).

[51] The errors quoted for the ratio $\sigma_\rho(Q^2,W)/\sigma_{\text{dif}}(Q^2,W)$ include the errors in $\sigma_\rho(0,W)$, $b_\rho$, and $R_\rho$ propagated to the ratio and added in quadrature.

[52] H. Fraas, Nucl. Phys. B36, 191 (1972).

[53] P. Joos *et al.*, Nucl. Phys. B122, 365 (1977).

[54] J. Martin *et al.*, Phys. Rev. Lett. 40, 283 (1978).

[55] When we fit the data in $Q^2$-$W$ bins to obtain cross sections as described in later sections, we fit the mass range $723 < m_{3\pi} < 843$ MeV. We also used phase space to help determine the shape of the background contribution at low $W$.

[56] P. G. O. Freund, Nuovo Cimento 48A, 541 (1967).

[57] V. Barger and D. Cline, Phys. Rev. Lett. 24, 1313 (1970).

[58] R. Dixon *et al.*, Phys. Rev. Lett. 39, 516 (1977).

[59] C. Berger *et al.*, Phys. Lett. 39B, 659 (1972).

[60] H. J. Besch *et al.*, Nucl. Phys. B70, 257 (1974).

[61] H. -J. Behrend *et al.*, Phys. Lett. 56B, 408 (1975).

[62] J. Orear, Report No. UCRL-8417, 1958 (unpublished); W. P. Swanson, Report No. DESY 66/17 (unpublished); W. P. Swanson *et al.*, Phys. Rev. 137, 1188 (1965).